第 54 卷第 2 期
2026 年 2 月

硅 酸 盐 学 报
JOURNAL OF THE CHINESE CERAMIC SOCIETY

Vol. 54，No. 2
February，2026

http://jccsoc.cbpt.cnki.net

**DOI**：10.14062/j.issn.0454-5648.20250458

综 合 评 述

# 中/高熵碳化物陶瓷及其基体/涂层改性碳/碳复合材料研究现状与展望

李佳宸[1]，张雨雷[1,2]，李 涛[2]，张 建[1]，付艳芹[2]，吕君帅[1]，李贺军[1]

(1. 西北工业大学，超高温结构复合材料重点实验室，西安 710072；2. 河南省科学院碳基复合材料研究院，河南省高性能碳纤维增强复合材料重点实验室，郑州 450046)

**摘 要**：碳/碳(C/C)复合材料超高温环境下的抗烧蚀性能提升是实现其作为高速飞行器热防护部件应用的前提。然而，传统硅化物及碳化物陶瓷改性 C/C 复合材料存在高温稳定性不足、长寿命抗烧蚀性能差及防护温区窄等问题。近年来，中/高熵碳化物(M/HEC)陶瓷独特的“四大效应”以及成分和微观结构的可调性，赋予了它们比传统硅化物及碳化物陶瓷更优异的综合性能，这为解决上述问题提供了新思路。本文综述了 M/HEC 陶瓷以及 M/HEC 基体/涂层改性 C/C 复合材料的制备方法及其对材料结构和性能的影响，概述了不同烧蚀组元对复合材料抗烧蚀性能的影响规律，并对 M/HEC 陶瓷及其改性 C/C 复合材料未来发展提出了展望。

**关键词**：碳/碳复合材料；中/高熵碳化物；基体/涂层改性；抗烧蚀性能
**中图分类号**：TB332；TQ174　　**文献标志码**：A　　**文章编号**：0454–5648(2026)02–0428–29
**网络出版时间**：2026–01–28



未来高速飞行器朝更快飞行速度、更长航时和更高稳定性的方向发展，其热防护系统不仅面临更高服役温度(>2000 ℃)以及由较大温度梯度引发的气动热载荷，还需承受高速气流/固体粒子冲刷导致的更强机械震动，这对用于热防护系统的热结构材料提出了更严苛的服役性能要求[1]。碳/碳(C/C)复合材料是以碳纤维($C_f$)为增强体的碳基复合材料，具有低密度(<2.2 g/cm$^3$)、高导热、高比强度、低热膨胀系数、尤其是高温惰性环境下力学性能随温度升高不降反升，甚至可在 2000 ℃以上仍保持较高力学性能等优势，被认为是可用于高速飞行器热防护系统最具前途的候选材料之一[2–3]。

自 1981 年以来，C/C 复合材料历经多次实际飞行验证，支撑欧美等国 40 余年的高速航天发展史，其中美国的 X-30、X-33、X-37B、X-43A、HTV-2 及 X-51A、日本的 HOPE-X、俄罗斯的“暴风雪”号和法国 Pro-X 等航天飞行器的不同热防护系统均使用了 C/C 复合材料[4, 5]。然而，C/C 复合材料在 450 ℃以上的氧化敏感性导致其力学性能急剧衰减，研究发现，当 C/C 复合材料氧化失重 1%和 10%后，其抗弯强度分别下降 10%和 30%左右，严重制约其在新一代高速飞行器热防护系统中的应用[6–8]。另外，C/C 复合材料在 2000 ℃以上有氧环境中会发生严重烧蚀，其中包括由超高温气流环境中的燃气介质($O_2$、$CO_2$ 及 $H_2O$ 等)引发的氧化反应，以及由气流压力和剪切力导致的材料剥蚀。目前，为提高 C/C 复合材料抗氧化/烧蚀性能，国内外研究学者将具有优异抗氧化/烧蚀性能的超高温陶瓷引入 C/C 复合材料并对其进行改性，通过充分整合 C/C 复合材料优异的高温力学性能和陶瓷优异的抗烧蚀性能，实现力学和抗烧蚀性能的协同提升，陶瓷改性 C/C 复合材料主要分为基体改性和涂层改性技术[9–11]。前者将一系列具有优异抗氧化/烧蚀性能的陶瓷材料引入低密度 C/C 复合材料中对其改性，通过氧化形成防护膜，覆盖 C/C 复合材料部分氧化/烧蚀活性位点；后者则在 C/C 复合材料表面制备陶瓷涂层，隔绝氧气与 C/C 复合材料基体直接接触，从而提高 C/C 复合材料抗氧化/烧蚀性能。

硅基陶瓷是目前研究最早、发展最成熟的抗氧化/烧蚀材料体系，主要包括 SiC[12–17]、$MoSi_2$[18–25]、

收稿日期：2025–06–11。　修订日期：2025–07–09。
基金项目：国家自然科学基金重点项目(52130205)；国家自然科学基金重大项目(52293373)。
第一作者：李佳宸(1997—)，男，博士研究生。
通信作者：张雨雷(1980—)，男，博士，教授。

**Received date:** 2025–06–11　**Revised date:** 2025–07–09.
**First author:** LI Jiachen (1997–), male, Doctoral candidate.
**E-mail:** lijiachen96@mail.nwpu.edu.cn
**Correspondent author:** ZHANG Yulei (1980–), male, Ph.D., Professor.
**E-mail:** zhangyulei@nwpu.edu.cn

$HfSi_2$[26, 27]、$CrSi_2$[28, 29]及 $ZrSi_2$[30, 31]等，其氧化产物 $SiO_2$ 具有低的氧扩散系数(1200 ℃时 $10^{-13}$ g·cm$^{-1}$·s$^{-1}$[32])和合适的黏度(1500 ℃时 $10^{7.95}$ Pa·s[8])，可在 1400~1600 ℃温区有效抑制氧气扩散，并保持良好流动性来愈合缺陷(孔洞和裂纹等)，从而延长 C/C 复合材料的使用寿命。然而，当面临 1700 ℃以上有氧环境时，硅化物的主动氧化能力增强，导致未氧化的硅基陶瓷形成气态 SiO 并逸出，同时 $SiO_2$ 的分解压以及饱和蒸汽压随温度升高而增加，加速氧化膜中已形成的 $SiO_2$ 分解并挥发，二者均会导致硅化物快速消耗，无法有效形成致密阻氧膜，逐步丧失热防护能力[33–35]。

超高温陶瓷是一种以共价键为主且熔点普遍高于 3000 ℃的化合物，因其具有优异的抗氧化烧蚀性能以及在 2000 ℃以上超高温环境下仍可保持化学稳定性等优势而广受青睐[36–40]。其中，HfC (~3890 ℃[41])和 ZrC (~3540 ℃[42])因具有更高熔点以及优异的化学稳定性，并且其氧化产物同样具备高熔点($HfO_2$：~2810 ℃[41]和 $ZrO_2$：~2670 ℃[43])，逐渐成为首选的碳化物热防护材料。但若只选择 HfC[44–51]、ZrC[52–55]和 HfC-ZrC[56–58]作为抗烧蚀组元，依旧难以实现对 C/C 复合材料的长寿命抗烧蚀防护，因为低熔点愈合相的缺失以及高温下 $CO/CO_2$ 的剧烈挥发导致氧化层呈多孔结构，阻氧性变差。为解决这一问题，本团队提出了多组元协同阻氧及低熔点自愈合缺陷的策略[7]，制备了 HfC/ZrC-SiC[59–68]、HfC/ZrC-NbC[69–71]、HfC/ZrC-TaC[72–80]和 HfC/ZrC-TiC[80, 81]等复相碳化物体系。高熔点固体氧化物颗粒($HfO_2/ZrO_2$)钉扎低熔点液相氧化物($SiO_2$：~1710 ℃[35]、$Ta_2O_5$：~1800 ℃[43]、$TiO_2$：~1840 ℃[81]和 $Nb_2O_5$：~1512 ℃[82])的复相结构，不仅增强了氧化膜的稳定性和抗冲刷能力，还促进了多组元氧化物互扩散发生固溶反应来愈合烧蚀缺陷，从而自生致密、高阻氧的氧化膜，C/C 复合材料抗烧蚀性能随之提升。然而复相碳化物在微观尺度到宏观尺度不均匀分布，导致烧蚀过程中局部富集的低熔点氧化物极易被机械剥蚀，因此大量烧蚀缺陷的形成以及低熔点愈合相的流失阻碍了 C/C 复合材料抗烧蚀性能进一步提高[83]。

与传统复相碳化物相比而言，中/高熵碳化物(M/HEC)陶瓷受益于热力学上的熵增、结构上的晶格畸变、动力学上的迟滞扩散和性能上的“鸡尾酒”效应，以及成分和微观结构的可调性，不仅保留了多组元协同效应，还具有微观尺度成分均匀性，展现出更优异的综合性能[84–90]。中/高熵碳化物陶瓷的出现为解决传统硅化物及碳化物陶瓷氧化膜阻氧能力不足、高温稳定性差和防护温域窄等难题提供了一条新途径。因此，实现高性能 M/HEC 基体/涂层改性 C/C 复合材料承载防护一体化设计与可控制备，可同步提升改性 C/C 复合材料在极端环境下的稳定承载及长寿命抗氧化/烧蚀性能。

本文梳理了近年来关于 M/HEC 形成能力预测、M/HEC 制备方法及 M/HEC 基体/涂层改性 C/C 复合材料制备方法的研究工作，着重对 C/C 复合材料抗烧蚀性能进行了总结与讨论，并结合当前科学技术发展趋势，指出了 M/HEC 基体/涂层改性 C/C 复合材料热结构材料面临的挑战及未来重点发展方向。

## 1　中/高熵碳化物陶瓷形成能力预测

受金属阳离子种类及各元素比例的影响，M/HEC 成分设计空间巨大，面对复杂的高维成分空间，仅采用传统的正交试验模式寻找理想的组元配比需要消耗大量精力和时间，从而直接导致材料的研制成本高、周期长，无法快速高效筛选单相 M/HEC 成分组合。研究人员正尝试通过理论计算结合高通量实验探索一种合理、有效且快速的方法来探究 M/HEC 单相形成能力并研究其综合性能，从而开发众多具有理想性能的 M/HEC 基体/涂层改性 C/C 复合材料。Gild 等[91]首次提出了以结构参数 $\delta$ 判据(晶格尺寸差，Lattice size difference)来预测单相高熵硼化物陶瓷(High-entropy boride，HEB)的单相形成能力，如式(1)所示。

$$\delta=\sqrt{\sum_{i=1}^{n}c_i\left(1-\frac{r_i}{\bar{r}}\right)^2} \tag{1}$$

式中：$n$ 为多组分固溶体的组元数；$c_i$ 为第 $i$ 个单元硼化物或碳化物的百分比；$r_i$ 为第 $i$ 个单元硼化物或碳化物的晶格常数；$\bar{r}$ 为组元硼化物或碳化物晶格常数平均值($\bar{r}=\sum_{i=1}^{n}c_ir_i$)。

HEB 体系中各组元原子半径差会影响各组元的固溶形成能力，较大差值不仅会导致体系内产生严重晶格畸变而引发高应变能，进而降低 HEB 相稳定性，还延缓了各组元间的互扩散速率，从而抑制单相形成。实验与计算结果证实，当 $\delta$<5.2%时，有利于形成 HEB[91]。$\delta$ 判据同样适用于 HEC 形成能力预测，Ye 等[85]计算所得$(Zr_{0.25}Nb_{0.25}Ti_{0.25}V_{0.25})C$ 的 $\delta$ 值为 4.59%，小于单相 HEB 形成 $\delta$ 阈值(5.2%)，因此形成单相$(Zr_{0.25}Nb_{0.25}Ti_{0.25}V_{0.25})C$ 理论可行，随

后均匀单相($Zr_{0.25}Nb_{0.25}Ti_{0.25}V_{0.25}$)C 的成功制备证实了这一结论。然而该方法仅从结构稳定性预测 HEC 形成能力，忽略了 HEC 制备阶段的热力学条件。因此 Ye 等[85, 92]还提出可借助计算吉布斯自由能变化($\Delta G_{mix}$)来评估 HEC 的热力学稳定性，如式(2)所示。

$$\Delta G_{mix} = \Delta H_{mix} - T\Delta S_{mix} \quad (2)$$

式中：$T$ 为绝对温度，K；$\Delta S_{mix}$ 和$\Delta H_{mix}$ 分别是混合物的熵和焓。

HEC 相较于传统陶瓷有更高的混合熵，这意味着体系自由能更低。考虑 C 原子占据的亚晶格对混合熵的贡献为 0，$\Delta S_{mix}$ 可表示为式(3)。

$$\Delta S_{mix} = -R/2\sum_{i=1}^{N} x_i \ln x_i \quad (3)$$

式中：$R$ 为理想气体常数(8.314 J·mol$^{-1}$·K$^{-1}$)；$x_i$ 为第 $i$ 种原子的摩尔分数。

由于温度对$\Delta H_{mix}$ 的影响较小，HEC 的$\Delta H_{mix}$ 近似于其在 0 K 下的$\Delta H_{mix}$，可表示为式(4)。

$$H_{mix}^{0K} = E - \sum_{i=1}^{n} E_{monocarbide}/n \quad (4)$$

式中：$E$ 和 $E_{monocarbide}$ 为 0 K 下弛豫后的 HEC 和单元碳化物能量；$n$ 为原子种类总数。

通过构型混合熵可使吉布斯自由能最小化，这有利于增强 HEC 的热力学稳定性。Ye 等[92]计算所得($Zr_{0.25}Nb_{0.25}Ti_{0.25}V_{0.25}$)C[85]和($Hf_{0.2}Zr_{0.2}Ta_{0.2}Nb_{0.2}Ti_{0.2}$)C 的热力学稳定临界温度分别为 25 ℃和 686 ℃，高温可促进均匀单相 HEC 形成。基于结构参数 $\delta$ 判据及热力学条件，Liu 等[93, 94]采用第一性原理计算了 HEC 弹性常数，借助经验公式推算各 HEC 熔点($T_m$=553+5.91$C_{11}$)，提出了新的热力学参数 $\Omega$ 判据($\Omega$=$T_m\Delta S_{mix}/\Delta H_{mix}$)。依据力学参数 $\Omega$ 判据、$\Delta H_{mix}$ 以及结构参数 $\delta$ 判据构建了 1 个包括 Ti、Zr、Hf、V、Nb、Ta、Mo 和 W 元素在内的 15 种四元以及 56 种五元 HEC 的三维相图(图 1[94])，研究了 HEC 形成能力及相稳定性，当满足 $\Omega$>1 且 $\delta$<6.6% ($\Omega$–$\delta$ 判据)时，可形成单相 HEC。

此外，Hossain 等[95]借助第一性原理计算提出了“价电子浓度”来预测 HEC 形成能力，结果表明，大多数 HEC 可在极高温度(>2700 ℃)保持稳定。该方法优点在于可预测高熵碳化物的热力学性质、晶格参数及无序态转变温度等，进而设计出具有优异综合性能的新型 HEC。Sarker 等[96]借助第一性原理计算提出能量分布谱，引入熵形成能力(EFA)，捕捉材料形成单相 HEC 晶体的相对倾向从而预测其 EFA，通过计算 56 种五元 HEC (Hf、Nb、Mo、Ta、Ti、V、W 和 Zr 组元) EFA 值，表明 EFA 的临界转变阈值为 50 eV$^{-1}$ (每个原子)，单相 HEC 形成能力随 EFA 增加而增强，并选取其中 9 种 HEC 进行实验验证，结果吻合良好，证明了该方法的有效性。

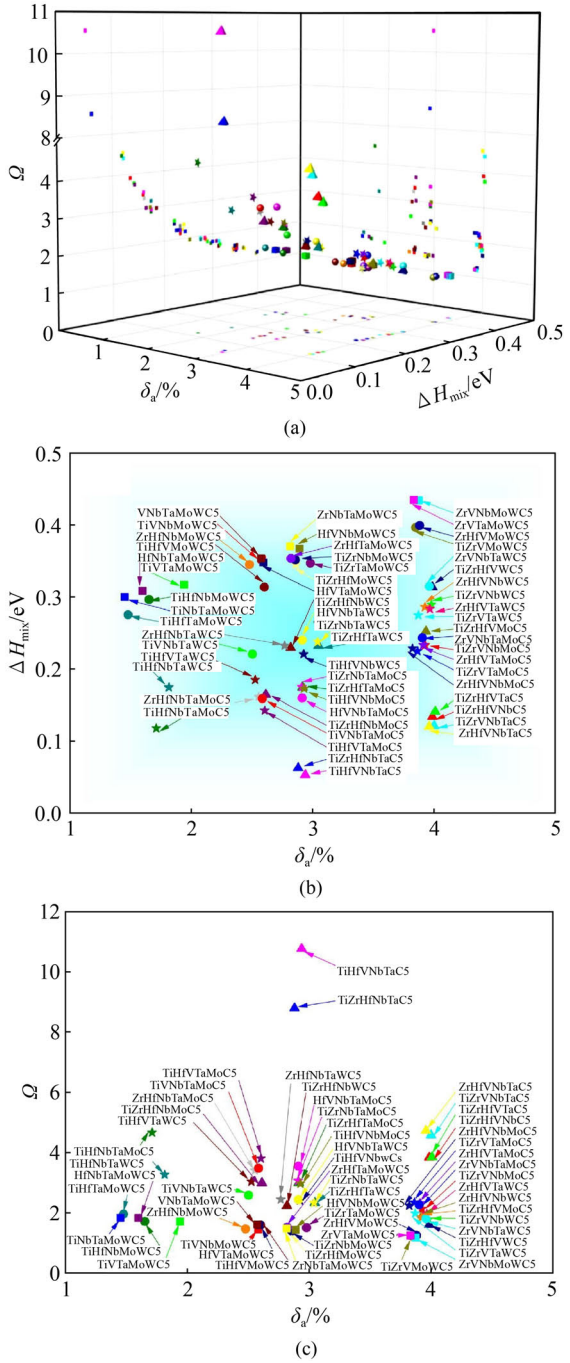



图 1 HEC 的(a) $\Omega$、$\Delta H_{mix}$ 和 $\delta$ 三维相图，(b) $\Delta H_{mix}$ 和 $\delta$ 以及(c) $\Omega$ 和 $\delta$ 的二维投影图[94]

Fig. 1 (a) Three-dimensional phase diagram in terms of $\Omega$, $\Delta H_{mix}$ and $\delta$; the corresponding two-dimensional projected maps of (b) $\Delta H_{mix}$ *versus* & $\delta$, (c) $\Omega$ *versus* & $\delta$ for HEC[94]

但上述方法仅通过单一判据预测 HEC 形成能力，预测精度极易受制备工艺及参数等外部条件影

响，具有一定局限性，并且缺乏高通量成分探索，无法深入挖掘 HEC 成分空间潜力。基于上述情况，Meng 等[97]整合上述判据，从材料物理性质参数、由组成 HEC 所扩展的 Hume-Rothery 规则参数及基本热力学参数 3 个方面将特征参数拓至 22 种，探索了可准确预测 HEC 形成能力的有效组合。如图 2 所示，首先借助焦耳加热高温设备高通量制备 91 个样本，结合 X 射线衍射分析(XRD)、扫描电子显微镜分析(SEM)和透射电子显微镜分析(TEM)辨别可形成单相 HEC 的成分组合，然后借助第一性原理获取 22 种特征参数作为机器学习前端数据集，通过机器学习数据集训练结合遗传算法优化特征集，实现最佳特征集合，从而提高预测数据与实验数据匹配精度，为后续预测未知 HEC 形成能力提供理论基础。

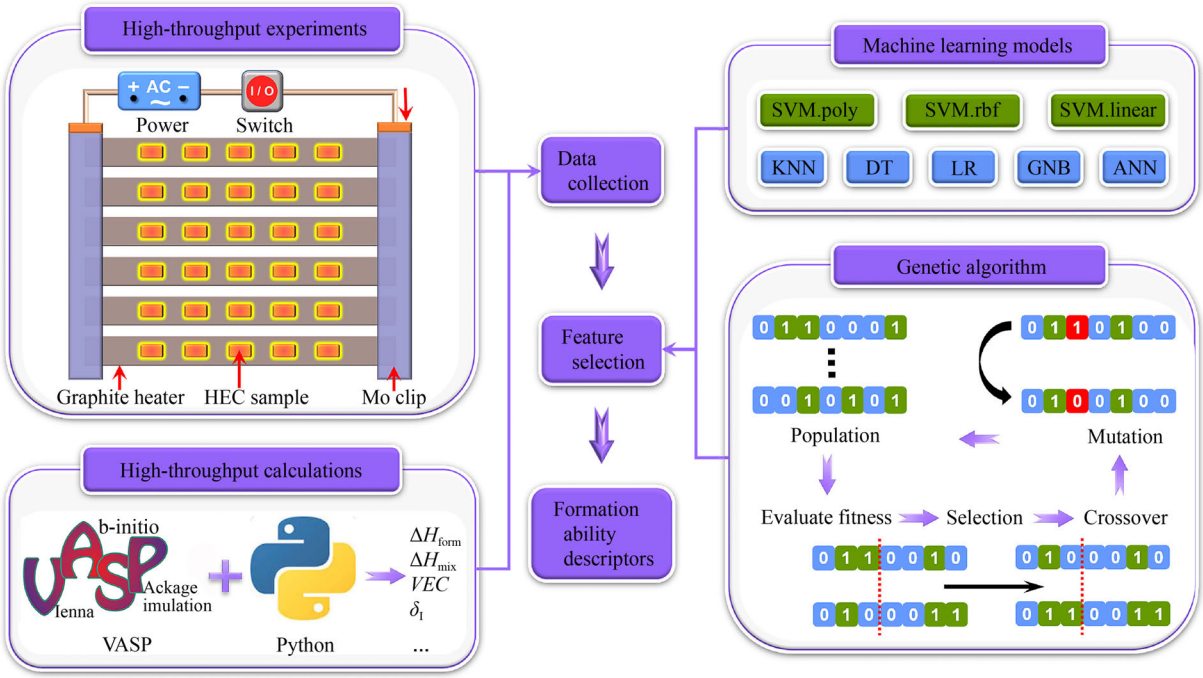



图 2　单相多组元碳化物形成能力预测流程图[97]

Fig. 2　Flowchart for establishing the formation ability descriptors of HEC[97]

## 2　中/高熵碳化物陶瓷制备现状

M/HEC 具有强的共价键以及低的晶格扩散系数，这限制了原子迁移率，因此 M/HEC 的制备需考虑不同工艺方法及工艺参数(时间、温度、粉料比例等)对所制备 M/HEC 的相组成、粒径形貌、元素分布、空位或间隙原子的组成及晶体结构等的影响[98–100]。目前，M/HEC 的制备主要分为固相反应法和液相反应法，其中固相反应法主要包括碳热还原法(CRM)、直接合成法(DSM)及熔盐法(MSS)，液相反应法主要包括聚合物转化陶瓷法(PDC，又称液相前驱体法)和溶胶凝胶法(SG)。

### 2.1　固相反应法

CRM 和 DSM 具有工艺简单、生产成本低、适合进行大规模工业生产等优势，已成为制备 M/HEC 最为常用且工艺最为成熟的方法，但加热温度高以及加工时间长极易导致晶粒粗大，此外还需要严格控制粉体纯度、热处理温度及热处理炉腔残余氧含量以避免引入氧杂质，因此对初始粉体粒径和纯度要求较高[101, 102]。相较于 CRM 和 DSM 需要较高的制备温度，MSS 则通过在反应原料中添加 KCl[103, 104]、NaCl[105]、$CaCl_2$[106, 107]等反应介质，借助其低熔点特性为反应原料提供液态环境，此时反应物在液相中的扩散活化能远小于固相中粉体的扩散活化能，从而降低可形成均匀单相 HEC 的反应温度[108]。

1) CRM 以金属氧化物粉末和石墨或碳粉为原料，经高温热处理实现 C 原子替代 O 原子形成单元碳化物，最终通过互扩散固溶形成单相 M/HEC 粉末(图 3[109])。Feng 等[110]以 $HfO_2$、$ZrO_2$、$TiO_2$、$Ta_2O_5$、$Nb_2O_5$和碳粉为原料，在 1900℃制得相对密度 99.3%和陶瓷粒径 1.2 μm 的(Hf-Zr-Ti-Ta-Nb)C 高熵陶瓷块体，借助 CRM 实现了高相对密度和细晶粒尺寸的 HEC 陶瓷制备工艺。受益于多组元固溶效应以及晶格畸变，(Hf-Zr-Ti-Ta-Nb)C 相较于单元碳化物陶瓷具有更优的力学性能。

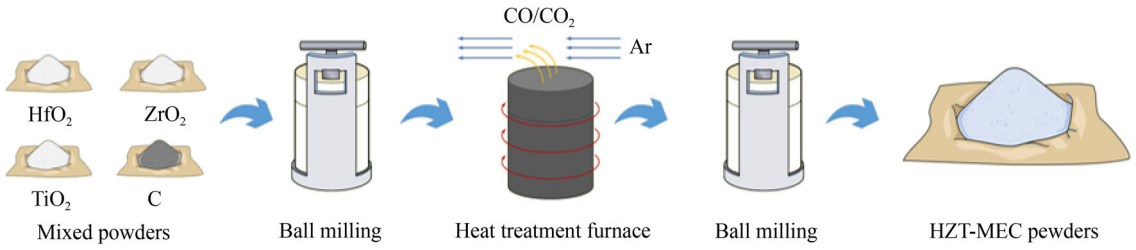



图 3 CRM 制备 MEC 粉末示意图[109]

Fig. 3 Schematic diagram of preparation of MEC powders by CRM[109]

在实际制备过程中，研究人员常通过调节 HEC 成分组元以及工艺参数，实现特定性能。Zhang 等[111]添加磁性元素来提高 HEC 电磁波吸收能力，以 $WO_3$、$Cr_2O_3$、$ZrO_2$、$TiO_2$、$Ta_2O_5$、$Nb_2O_5$、$Ni_2O_5$ 和石墨为原料，在 1900 ℃制得(WZrNbTaCr)C 和(WZrNbTaNi)C 粉末，结果显示，二者阻抗匹配和电磁波衰减能力都得到了增强，从而提高了它们的吸波性能。他们还借助纳米增韧效应，在此基础引入 SiC 纳米线($SiC_w$)，通过两步快速热压烧结法制备(WZrNbTaTi)C-$SiC_w$ 陶瓷块(制备流程如图 4[111]所示)，从而提高其力学性能。

作者前期以 $HfO_2$、$ZrO_2$、$TiO_2$、$Ta_2O_5$ 和碳粉为原料，通过调节制备温度(1700~2100 ℃)，制备了不同比例的(Hf-Zr-Ti)C 粉末和(Hf-Zr-Ta-Ti)C 粉末，分析高温下不同金属阳离子间的相互反应扩散过程，随后将其作为抗烧蚀涂层制备于 C/C 复合材料表面，并研究其抗烧蚀性能[109, 113–115]。以$(Hf_{0.25}Zr_{0.25}Ti_{0.5})C$ 为例，实验结果显示，随温度增加，原子尺寸差异引起富 Hf-Zr 碳化物优先形成，随后富 Ti/Ta 碳化物与之相互固溶，最终于 2100 ℃形成均匀单相$(Hf_{0.25}Zr_{0.25}Ti_{0.5})C$ 粉体(图 5[114])。受益于多组元协同阻氧优势，(Hf-Zr-Ti)C 和(Hf-Zr-Ta-Ti)C 均表现出较好的抗烧蚀性能。

2) DSM 以多种碳化物粉末为原料，结合无压(PS)[10, 116]、热压(HPS)[117, 118]或放电等离子烧结(SPS)[119–122]工艺制备 M/HEC 陶瓷。Yu 等[116]以单元碳化物粉末为原料、酚醛树脂为黏合剂，借助 PS 辅助 DSM 在 2200 ℃保温 2 h 制得$(Hf_{0.2}Zr_{0.2}Ta_{0.2}Nb_{0.2}Ti_{0.2})C$ 块体，分析了酚醛树脂衍生碳含量对其密度、力学和热性能的影响。然而 PS 制备时间长，HPS 可显著缩短其制备时间。Sun 等[118]以 HfC-TaC-ZrC-NbC-TiC 复相粉末为原料，借助 DSM 结合 HPS 在 1800~1950 ℃和 30 MPa 烧结 30 min，制备均匀单相$(Hf_{0.2}Ta_{0.2}Zr_{0.2}Nb_{0.2}Ti_{0.2})C$ 陶瓷块体(图 6[118])，通过界面处的原子扩散和化学反应获得了具有高剪切强度的固体接头。

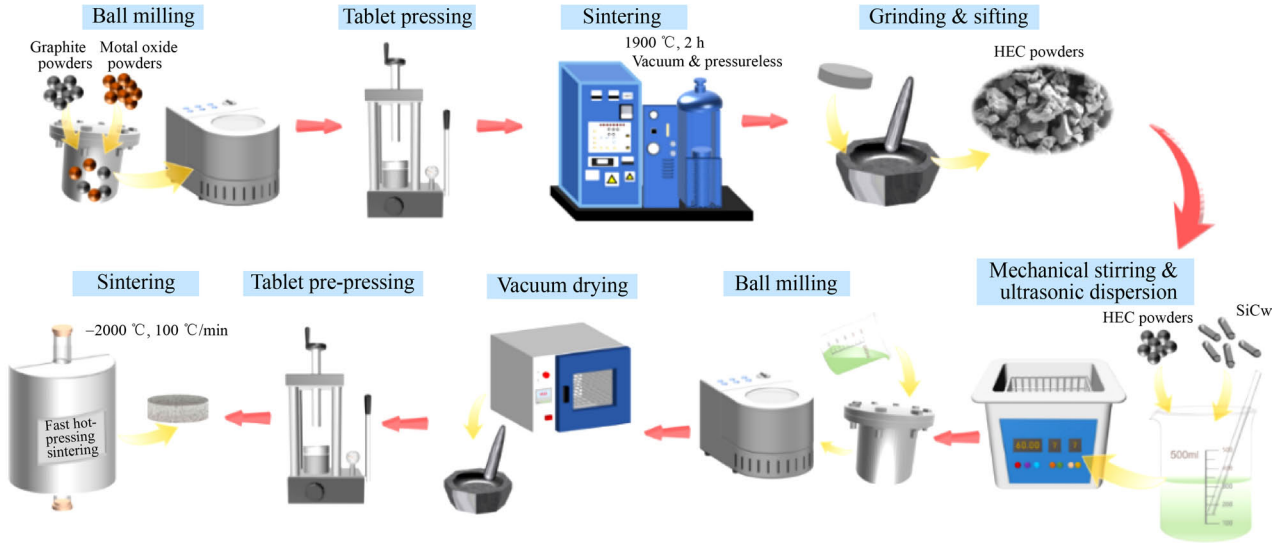



图 4 (WZrNbTaNi)C-SiCw 复合材料的制备示意图[111]

Fig. 4 Schematic for the preparation of (WZrNbTaNi)C-$SiC_w$ composites[111]

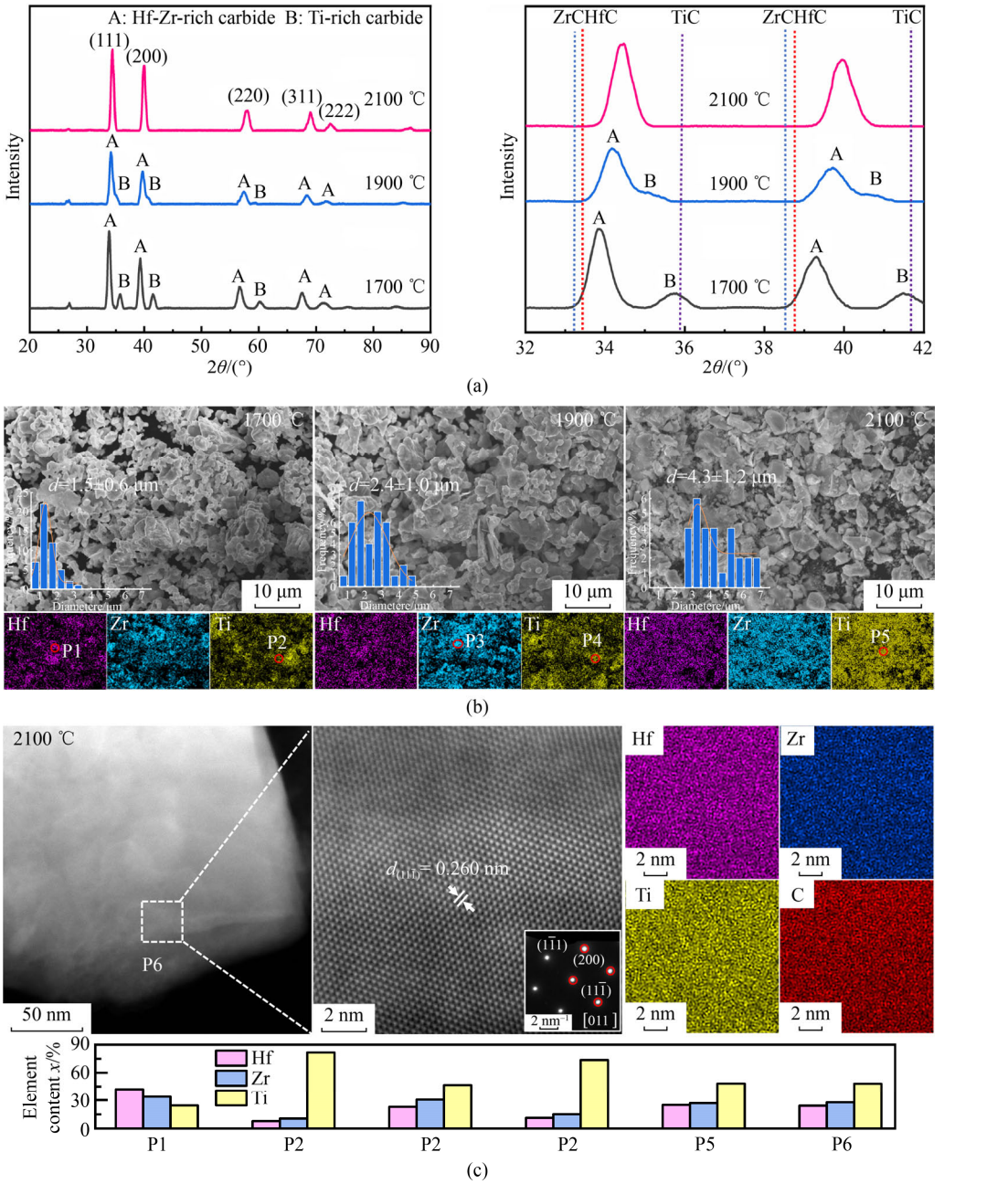



图 5　不同温度合成$(Hf_{0.25}Zr_{0.25}Ti_{0.5})C$ 粉末的(a) XRD 谱，(b) SEM 和(c) 2100 ℃时的 TEM 照片[114]

Fig. 5　(a) XRD pattern, (b) SEM, and (c) TEM images at 2100 ℃ of $(Hf_{0.25}Zr_{0.25}Ti_{0.5})C$ powders prepared at different temperatures[114]

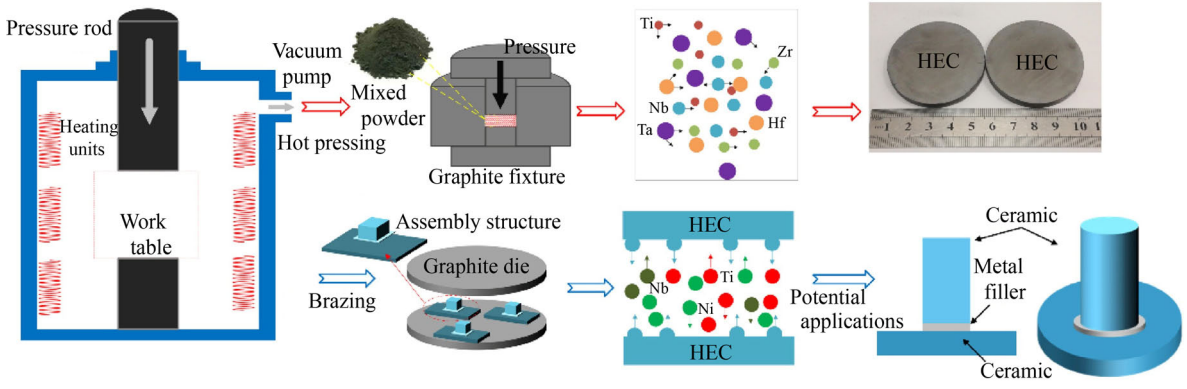



图 6　$(Hf_{0.2}Ta_{0.2}Zr_{0.2}Nb_{0.2}Ti_{0.2})C$ 的热压烧结和主动钎焊示意图[118]

Fig. 6　Schematic diagram of HP sintering and active brazing of $(Hf_{0.2}Ta_{0.2}Zr_{0.2}Nb_{0.2}Ti_{0.2})C$[118]

SPS 烧结通过在电极上施加高脉冲电流(图 7[123]),在粉末颗粒间隙中的放电产生等离子体，可有效消除粉末颗粒表面吸附性气体和杂质，破坏颗粒表面氧化膜，从而增强烧结材料的热扩散能力，显著提高制备效率[119]。Peng 等[121]以 5 种碳化物为原料，采用高能球磨结合 SPS 在 2000 ℃制备$(Ta_{0.2}Hf_{0.2}Zr_{0.2}Ti_{0.2}Nb_{0.2})C$ 陶瓷块体，并研究其抗烧蚀性能。Zhang 等[120]采用 SPS 辅助 DSM 在 1950 ℃合成(TiZrHfNbTa)C 陶瓷块体，结合第一性原理计算，对其电子性质、热力学稳定性和力学性质进行了深入研究。Liu 等[124]在 SPS 基础上开发出放电等离子耦合高频感应烧结(SPS-HF)，该方法可产生高能环境，提供充足活化能来促进原子克服能垒，通过 DSM 结合 SPS-HF 在 1350℃下成功制备了(W, Nb, Mo, Ta, Ti)C 高熵陶瓷，显著降低制备温度。实验结果显示高强度磁性金属黏结相(Co、Ni)的高频感应烧结效应，利用空位机制和金属液相，较短时间内实现各相快速扩散，从而实现低温制备致密 HEC 陶瓷(图 8[124])。

3) MSS 制备 M/HEC 分为以下 4 个阶段：混合氧化物、石墨和熔盐(图 9a)，熔盐熔化及反应物重排(图 9b)，熔盐介质间的互扩散以及石墨表面的反应(图 9c)，M/HEC 的形核与生长(图 9d 和图 9e)[104, 106]。Ning 等[104]以 Ta、Nb、Ti 和 V 金属粉末以及 C 粉末为原料，KCl 为反应介质，借助 MSS 在 1300 ℃首次合成$(Ta_{0.25}Nb_{0.25}Ti_{0.25}V_{0.25})C$ 纳米粉末，该粉末具有单晶面心立方结构以及从纳米级到微米级的

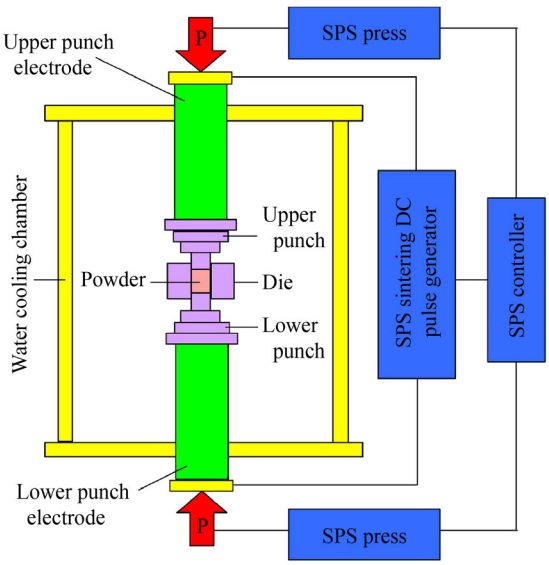



图 7 SPS 过程示意图[123]]

Fig. 7 A schematic of the SPS process[123]

均匀成分分布。An 等[105]以 Ta、Nb、Ti 和 V 金属粉末和 C 粉末为原料，KCl 和 NaCl 为反应介质，在 1400 ℃制备出粒径约为 400 nm 的均匀单相(TaNbTiV)C 纳米粉末。MSS 工艺不仅可制备高纯纳米粉末，还可用于块体制备。Ma 等[106]则以 $CaCl_2$ 为反应介质，借助 MSS 将 $Ta_2O_5$、$Nb_2O_5$、$TiO_2$、$V_2O_5$ 和 C 粉末于 1500℃合成高纯度片状(TaNbTiV)C。

MSS 法最大优势在于其可显著降低反应所需温度，提供低黏度的液态反应环境，增强反应物的扩散速率与接触效率，从而形成目标产物。熔盐中的离子环境有助于原料的电离与活化，提升反应驱

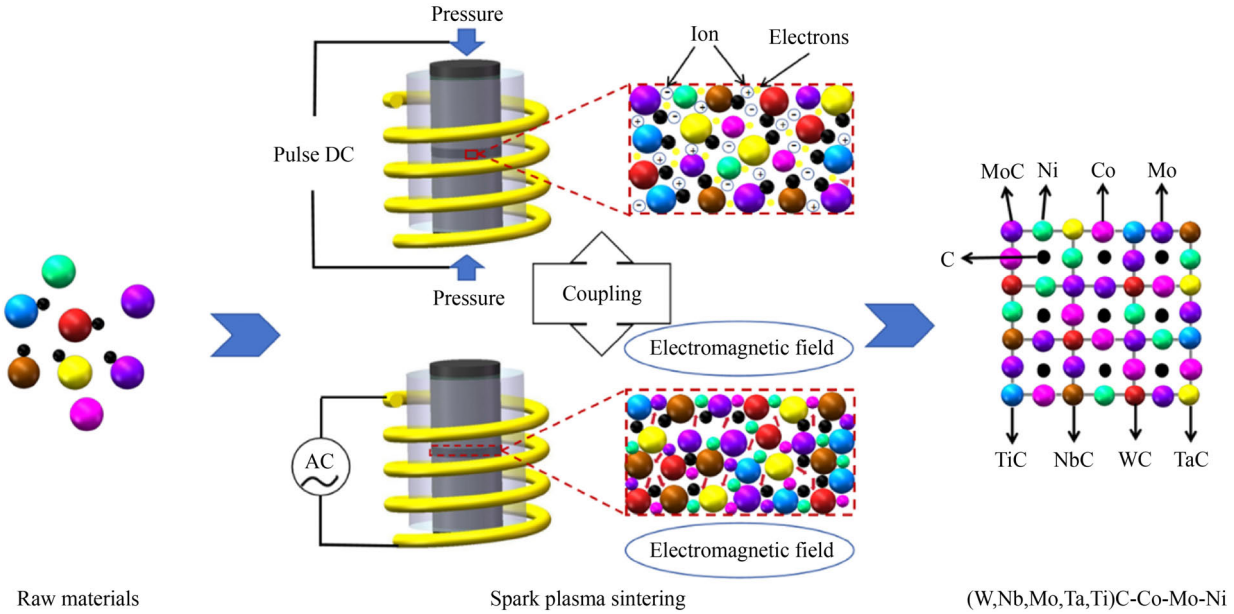



图 8 放电等离子耦合高频感应制备高熵(W, Nb, Mo, Ta, Ti)C 高熵陶瓷示意图[124]

Fig. 8 Schematic drawing of high-entropy (W, Nb, Mo, Ta, Ti)C cermet by SPS-HF sintering[124]

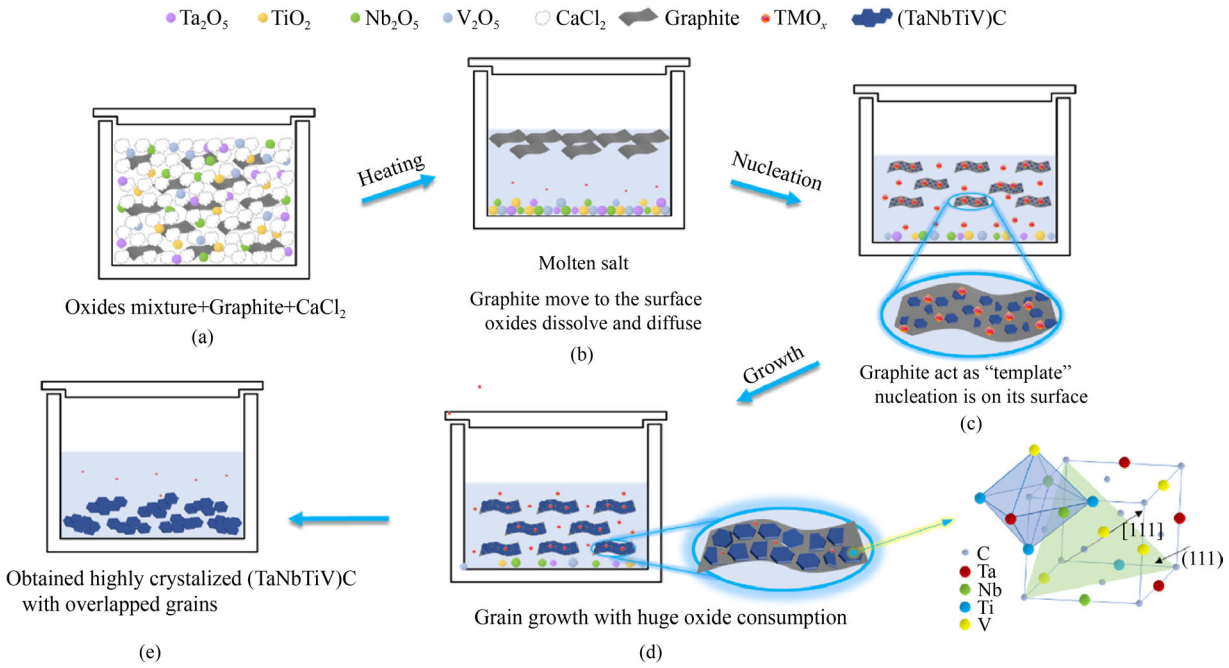



图 9　熔融盐介质中(TaNbTiV)C 形成过程示意图：(a)原料混合，(b)熔融盐中反应物重排，(c)熔融盐介质中的扩散和石墨表面的反应，(d)和(e)晶粒粗化和片状(TaNbTiV)C 形成[106]

Fig. 9　Formation schematic of t the (TaNbTiV)C in molten salt medium: (a) mixing of the raw materials, (b) re-arrangement of the reactants in molten salt, (c) diffusion in molten salt medium and reation on the surface of graphite, (d) and (e) grain coarsening and forming flake like (TaNbTiV)C[106]

动力和产物的结晶质量。该方法合成的 M/HEC 不仅分散性良好、物相纯度高，还可通过调控熔盐种类、比例精准调控产物的形貌和尺寸，从而赋予产物独特的结构与性能。然而，熔盐体系在高温下具有一定腐蚀性，容易侵蚀坩埚及相关反应设备。

### 2.2　液相反应法

相较于固相反应法所需较高反应温度和较长保温时间，研究人员开发了制备条件更温和的液相反应法，主要包括 PDC 和 SG，二者均可有效降低反应温度，合成具有纳米级粒径的纯净单相 HEC 粉体。尽管二者都历经液相前驱体转化陶瓷过程，但 PDC 无凝胶化，仅通过高温挥发，稠状物质黏度低，可塑形能力弱，常用作制备离散多孔纳米颗粒；而 SG 核心在于凝胶化，所得胶体黏度高，可塑形能力强，常用作构建网络结构，适合制备多孔连续材料。

1) PDC 工艺不仅可提高陶瓷成分均匀性，还可制备复杂成分，但易受温度影响。Du 等[125]借助 PDC 在 2200 ℃成功合成平均粒径约为 800 nm 的超细 $(Hf_{0.25}Nb_{0.25}Zr_{0.25}Ti_{0.25})C$ 纳米粉末，实现了纳米级到微米级的高成分均匀性，该纳米粉末具有极低氧杂质含量和游离碳杂质含量。Sun 等[126, 127]不仅通过该方法在 1800 ℃成功制备了 8 种新型高纯 HEC 纳米粉末，还研究了不同制备温度对裂解产物物相的影响(制备流程如图 10[126]所示)。实验结果显示 1000 ℃以下主要以氧化物为主，随温度的增加，碳化物逐渐形成，并于 1400 ℃出现少量 HEC，最终于 1800 ℃成功制备了(Ti, Zr, Hf, Ta)C、(Ti, Zr, Hf, Ta)C、(Ti, Zr, Hf, Mo, W)C、(Zr, Hf, Ta, Mo, W)C、(Ti, Zr, Hf, Ta, La, Y)C、(Ti, Zr, Hf, Ta, Nb, Mo, W)C、(Ti, Zr, Hf, Ta, La, Y)C 和(Ti, Zr, Hf, Ta, Nb, Mo, W, La)C。

本团队 Zhao 等[128]引入二乙烯基苯降低高熵陶瓷固溶温度，借助 PDC 在碳布上成功制备了单源前驱体衍生的$(Ti_{0.2}Zr_{0.2}Hf_{0.2}Nb_{0.2}Ta_{0.2})C$ 纳米线(图 11[128])，合成了多分支、单分支和单分支弯曲状的形貌可控纳米线，并证明了纳米线的生长模型为顶端型气–液–固机制，表明单源前驱体衍生一维纳米材料在高温下受典型的瑞利不稳定性影响发生几何变形。本团队 Li 等[129]还采用 PDC 制备了新型 $HfC_xN_{1-x}$ 陶瓷粉末(图 12[129])，该方法合成的前驱体具有良好化学稳定性，热处理后制备出的陶瓷粉末可在纳米尺度上实现元素均匀分布，可为后续研制并合成高熵碳氮化物奠定理论基础，但是该工艺过程烦琐较难实现陶瓷大批量生产。

2) SG 一般采用金属醇盐水解形成溶液，缩合形成溶胶(显著丁达尔效应)，然后凝胶化来固化混

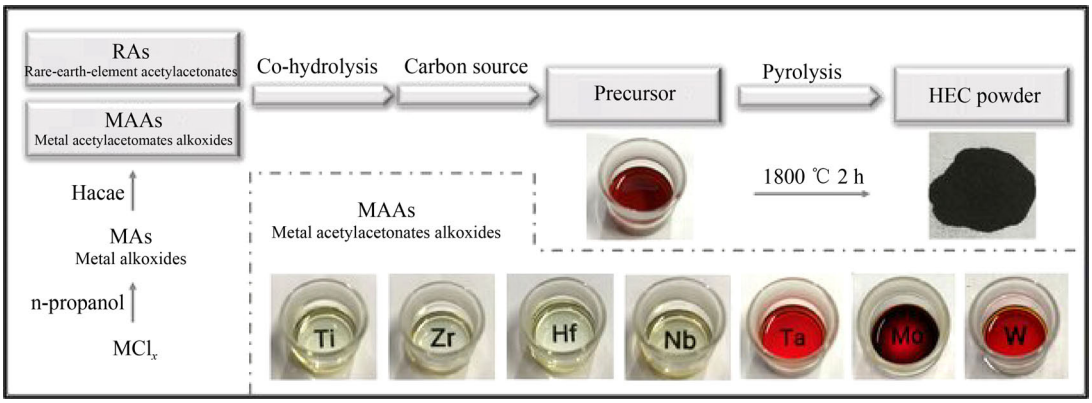



图 10 液相聚合物前驱体和陶瓷粉末的合成流程示意图[126]

Fig. 10 Schematic diagram of the synthesis procedure for liquid polymer precursors and ceramic powders[126]

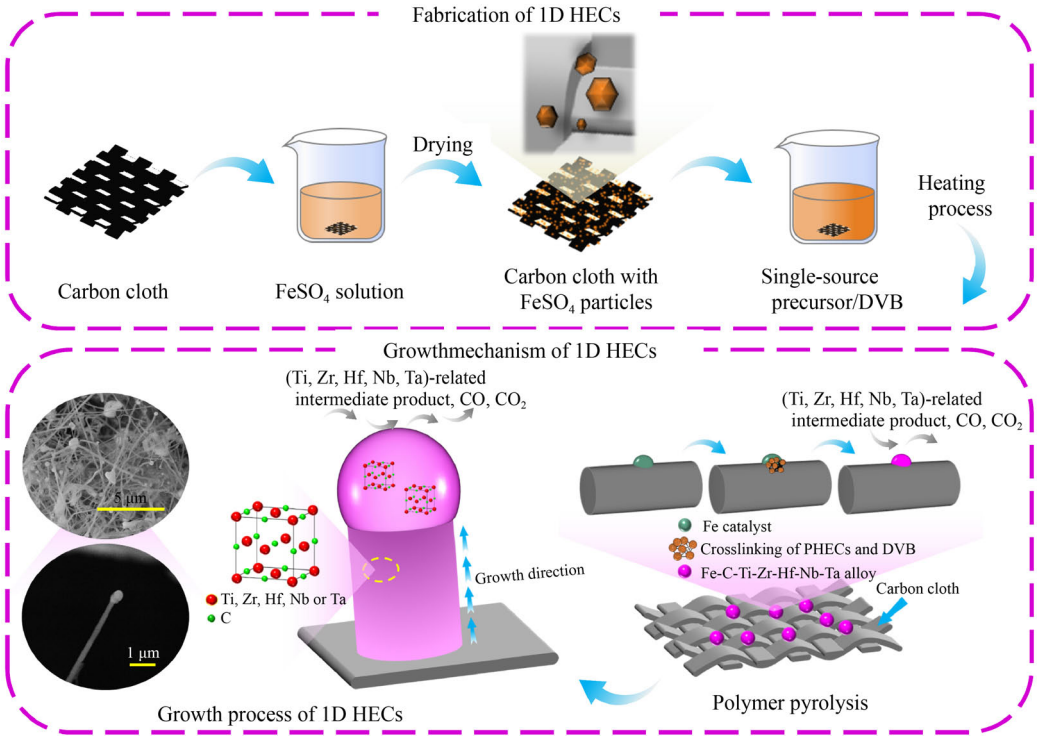



图 11 前驱体制备$(Ti_{0.2}Zr_{0.2}Hf_{0.2}Nb_{0.2}Ta_{0.2})C$ 示意图[128]

Fig. 11 Fabrication schematic of $(Ti_{0.2}Zr_{0.2}Hf_{0.2}Nb_{0.2}Ta_{0.2})C$ nanowires[128]

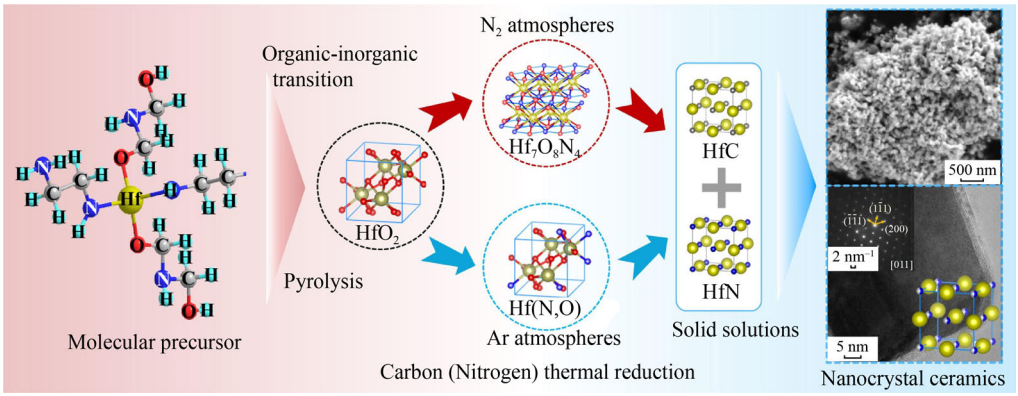



图 12 $HfC_xN_{1-x}$ 前驱体的合成和裂解过程示意图[129]

Fig. 12 Schematic of the synthesis and pyrolysis process of $HfC_xN_{1-x}$ precursor[129]

合体，最后通过热处理或掺杂处理以形成固体 HEC 粉体，所制备粉末具有高纯度和良好化学均匀性。该工艺可通过调节分散剂比、pH 值等参数精细控制粒径和形状，但易受 pH 值影响[130]。Wang 等[131]借助 SG 设计并合成$(Ti_{1/3}Zr_{1/3}Ta_{1/3})C$、$(Ti_{1/3}Zr_{1/3}Hf_{1/3})C$和$(Ti_{1/4}Zr_{1/4}Ta_{1/4}Hf_{1/4})C$粉体，液相前驱体在 800 ℃裂解，随后在超过 1800 ℃的温度下形成均匀的 FCC 固溶体，粉末粒径分别为 340、248 nm 和 401 nm。其形成机理如图 13 所示，首先金属离子与柠檬酸络合形成 Zr-Ti 凝胶(图 13a)，然后添加 $HfO_2$ 和 $Ta_2O_5$ 氧化物粉末促进干凝胶均匀分散，待干凝胶裂解后形成氧化物和碳的混合前驱体(图 13b)，逐渐升温，前驱体经历碳热还原和固溶反应，最终形成目标粉体(图 13c)。

Zhang 等[132]还结合 SG 和 CRM 合成了一种新型$(Hf_{0.2}Zr_{0.2}Ti_{0.2}Ce_{0.2}La_{0.2})C_{1-\delta}$陶瓷纳米颗粒。如图 14 所示，首先在去离子水中混合葡萄糖和超细$(Hf_{0.2}Zr_{0.2}Ti_{0.2}Ce_{0.2}La_{0.2})O_x$ (后续简称 HEFO)，葡萄糖于 500 ℃开始转化为多孔无定形碳，然后超细 HEFO 颗粒附着于多孔葡萄糖衍生的碳结构；1200~1300 ℃碳热还原反应开始，产生的气态 HEFO [图 14 中式(2)]与葡萄糖接触并反应形成包含 HEC

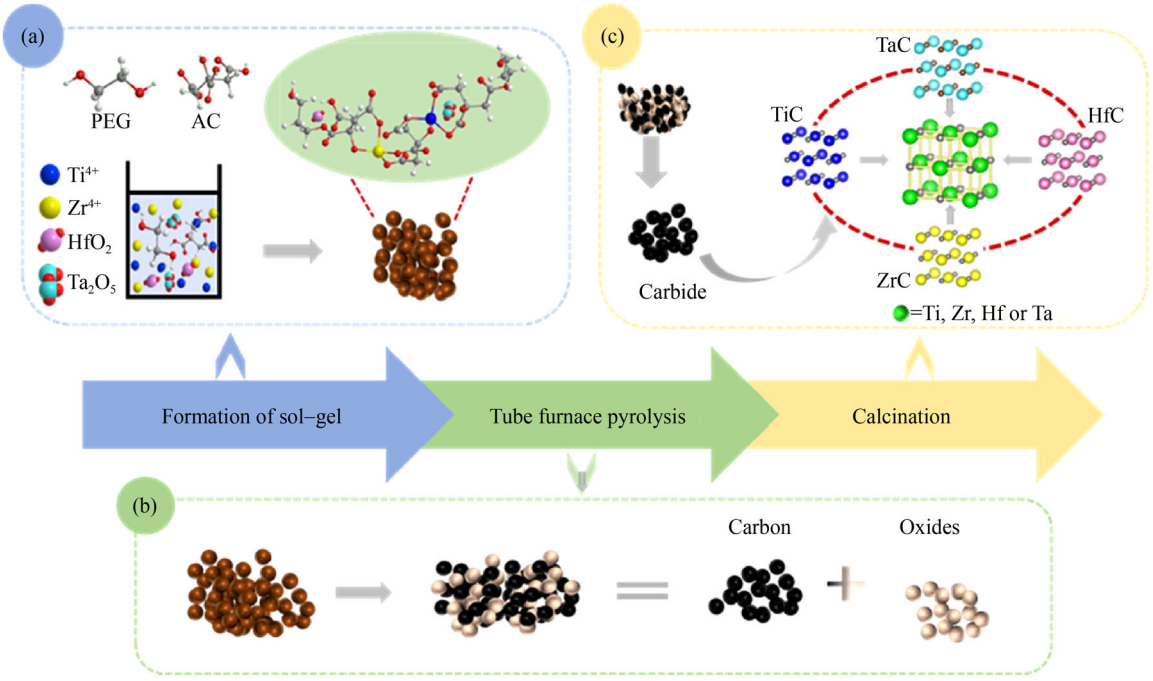



图 13　SG 合成 HEC 陶瓷粉体机理图：(a)溶胶–凝胶阶段，(b)干凝胶热解阶段，(c)前驱体的碳热还原和固溶阶段[131]

Fig. 13　Synthesis mechanism diagram of HEC ceramic powders by SG: (a) sol–gel process, (b) pyrolysis process of dry gel, (c) carbothermal reduction and solid solution processes of the precursor[131]

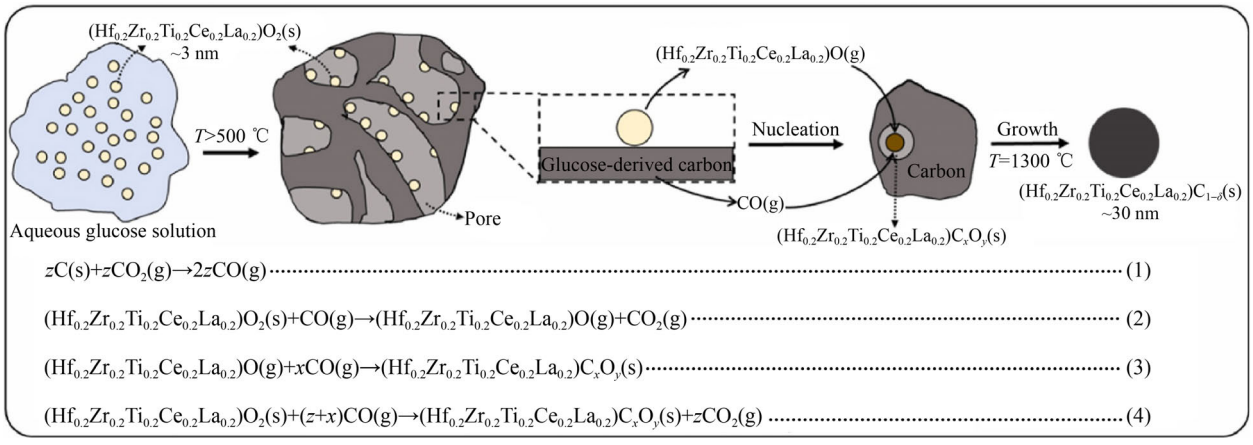



图 14　葡萄糖制备 HEC 粉末示意图[132]

Fig. 14　Schematic of preparing HEC powders by glucose[132]

核和非晶外壳的碳氧非晶核壳结构；最终于 1500 ℃实现了 30 nm 超细单相$(Hf_{0.2}Zr_{0.2}Ti_{0.2}Ce_{0.2}La_{0.2})C_{1-\delta}$。Zhang 等[133]采用 SG 合成了不同碳源(葡萄糖)的(FeCoCrMnNi)C，随碳源含量增加，孔隙更加丰富，呈网状分布，该工作为电化学超级电容器电极材料的开发提供了新的策略。

## 3 中/高熵碳化物陶瓷基体/涂层改性 C/C 复合材料的制备现状

上述 M/HEC 前驱体和粉体可为 M/HEC 基体/涂层改性 C/C 复合材料的制备提供液体和固体原料，所设计 M/HEC 的成分、元素比例、晶粒尺寸及组织结构为构建 M/HEC 基体/涂层改性 C/C 复合材料提供了理论依据和技术支撑。M/HEC 基体/涂层改性 C/C 复合材料不仅整合了 M/HEC 的高熔点与优异高温化学稳定性，以及 C/C 复合材料的低密度、高导热性和优异高温惰性力学保持率等优点，还受益于其巨大的成分、组织和结构设计空间而具有更广阔的性能潜力。

### 3.1 基体改性方法

目前 M/HEC 基体改性 C/C 复合材料(后续简称 C/C-M/HEC)的工艺主要包括前驱体浸渍裂解(PIP)工艺和反应熔渗(RMI)工艺。PIP 工艺可制备均匀分布的纳米级陶瓷，且具有高渗透深度等优点，然而前驱体在裂解过程中容易发生体积收缩，在材料内部形成裂纹和孔隙，并且前驱体浸渍效率会随着浸渍次数增加而降低，成本高、制备周期长[134]。与 PIP 工艺相比，RMI 工艺成本更低、效率更高，还可制备复杂几何形状部件，但极易因较高的制备温度损坏 $C_f$ 而导致 C/C 复合材料力学性能下降[135]。

1) PIP 工艺借助特定 HEC 陶瓷聚合物前驱体溶液浸渍低密度 C/C 复合材料，然后热处理转化形成 HEC 陶瓷。Song 等[136]采用前文 Sun 等[126, 127]所述 PDC 工艺合成了$(Hf_{1/2}Zr_{1/3}Ti_{1/6})C$ 液相前驱体，随后借助 PIP 裂解制得 $C_f/(Hf_{1/2}Zr_{1/3}Ti_{1/6})C$ 复合材料，并研究其力学和抗烧蚀性能。Zhang 等[137]借助 PIP 制备了 C/C-(Ti, Zr, Hf)C-SiC 和 C/C-(Ti, Zr, Hf, Ta)C-SiC 复合材料(流程如图 15 所示)。(Ti, Zr, Hf)C 液相前驱体于 1400 ℃完全分解形成富 Hf-Zr 碳化物和富 Ti 碳化物，并于 2200 ℃形成单相(Ti, Zr, Hf)C。由于 TaC 具有最低空位形成能，不仅能加速与 TiC 形成富 Ti-Ta 碳化物，还可加速其与富 Hf-Zr 碳化物固溶形成(Ti, Zr, Hf, Ta)C，从而降低其单相形成温度，因此单相(Ti, Zr, Hf, Ta)C 形成于 2000 ℃。

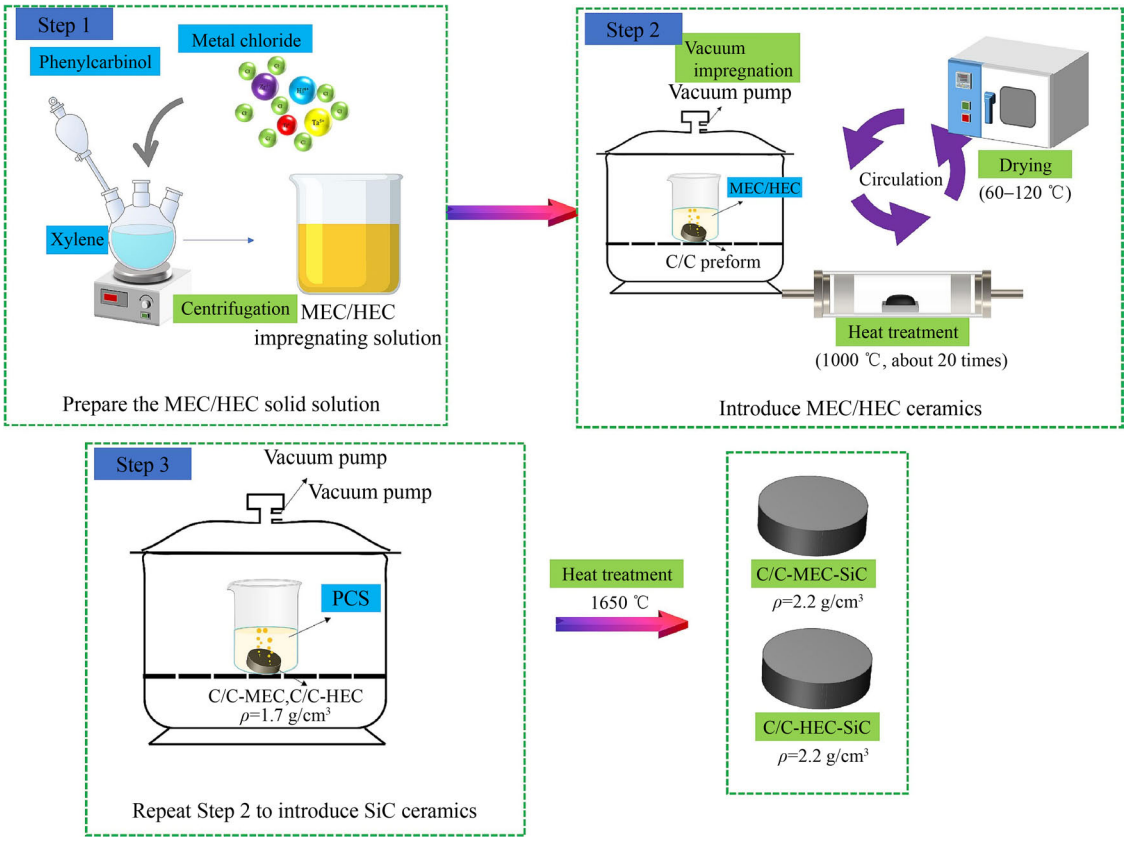



图 15 C/C-MEC-SiC 和 C/C-HEC-SiC 复合材料的制备流程图(MEC is (Ti, Zr, Hf)C；HEC is (Ti, Zr, Hf, Ta)C)[137]

Fig. 15 Preparation flow chart of C/C-MEC-SiC and C/C-HEC-SiC composites (MEC is (Ti, Zr, Hf)C; HEC is (Ti, Zr, Hf, Ta)C)[137]

Cai 等[138–140]以$(Ti_{0.2}Zr_{0.2}Hf_{0.2}Nb_{0.2}Ta_{0.2})C$前驱体和聚碳硅烷为原料，采用 PIP 向 3D C/C 复合材料引入$(Ti_{0.2}Zr_{0.2}Hf_{0.2}Nb_{0.2}Ta_{0.2})C$和 SiC。HEC 液相前驱体历经单元氧化物碳热还原形成单元碳化物，随后单元碳化物固溶形成 HEC，于 1700 ℃时成功制备$C_f/(Ti_{0.2}Zr_{0.2}Hf_{0.2}Nb_{0.2}Ta_{0.2})C$-SiC 复合材料(图 16)[138]。HEC 的成功引入确保该复合材料具有优异的抗弯强度(322MPa)和断裂韧性(8.24 $MPa·m^{1/2}$)。Cai 等还测试了$C_f/(Ti_{0.2}Zr_{0.2}Hf_{0.2}Nb_{0.2}Ta_{0.2})C$-SiC 复合材料在热通量为 4 $MW/m^2$[140]和 5 $MW/m^2$[138, 139]的等离子烧蚀性能，结果显示该复合材料表现出优于传统复相陶瓷的抗烧蚀性能。

本团队 Miao 等[141]和 Fu 等[142]以 HfC-TaC-ZrC 复相碳化物前驱体为阳离子源，采用 PIP 工艺于 1900 ℃制备出不同 Hf、Ta 和 Zr 摩尔比的 C/C-(Hf-Ta-Zr)C 和不同 SiC 含量的 C/C-(Hf-Ta-Zr)C-SiC (流程如图 17[141]所示)。(Hf-Ta-Zr)C 陶瓷相在低密度 C/C 复合材料基体内部均匀分布，无较大孔隙缺陷

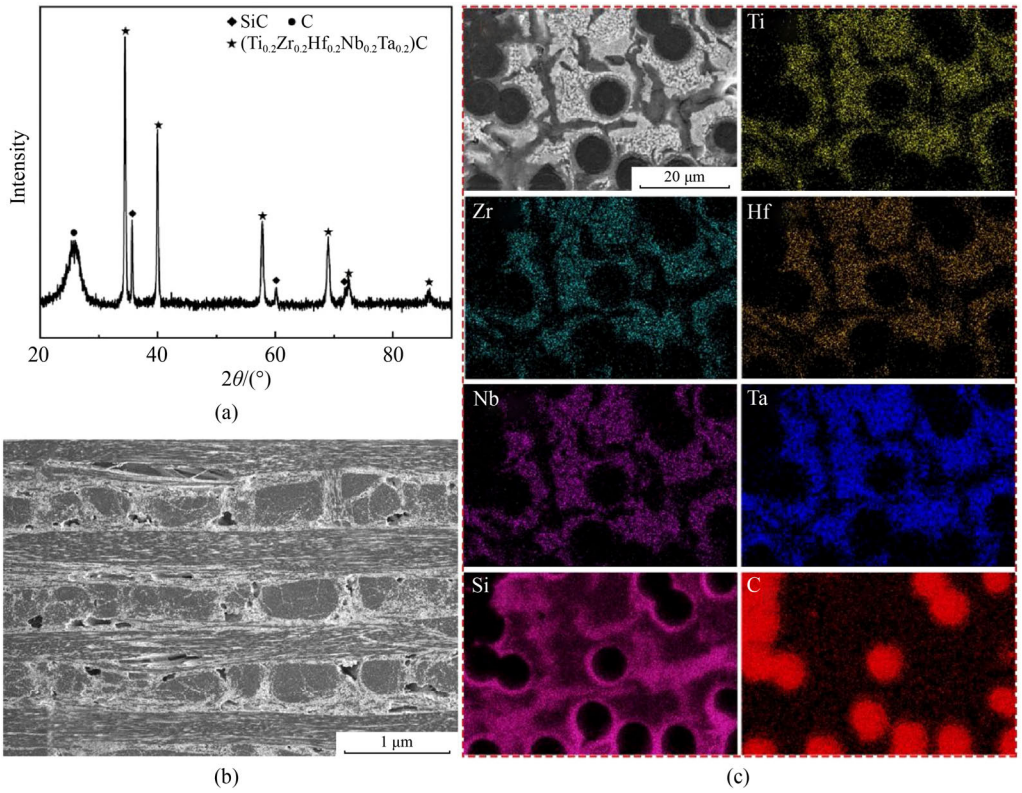



图 16　$C_f/(Ti_{0.2}Zr_{0.2}Hf_{0.2}Nb_{0.2}Ta_{0.2})C$-SiC 复合材料(a) XRD 谱，(b) SEM 照片和(c) EDS 谱[138]

Fig. 16　(a) XRD pattern, (b) SEM image and (c) EDS spectra of $C_f/(Ti_{0.2}Zr_{0.2}Hf_{0.2}Nb_{0.2}Ta_{0.2})C$-SiC composites[138]

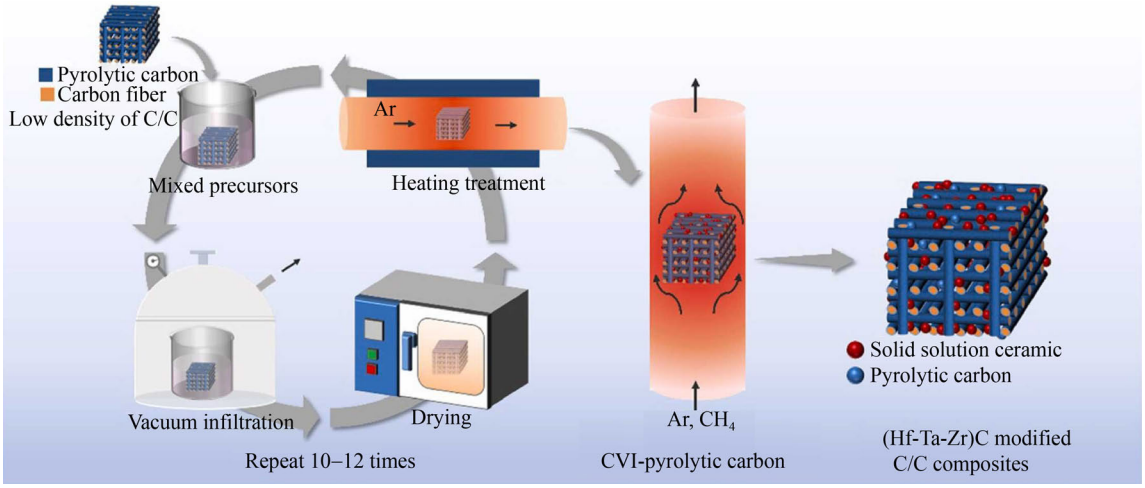



图 17　C/C-(Hf-Ta-Zr)C 制备工艺示意图[141]

Fig. 17　Schematic diagram of C/C-(Hf-Ta-Zr)C fabrication process[141]

和结壳现象。随后研究了不同元素比例和 SiC 含量对改性后 C/C 复合材料力学性能、热物理性能以及抗烧蚀性能的影响。

2) RMI 工艺制备 C/C-M/HEC 常采用金属单质粉体或 M/HEC 合金粉体作为阳离子源，通过高温熔渗至基体内部，并与基体内 $C_f$或热解碳反应生成 HEC。Gao 等[143]将 Hf、Zr 和 Ti 金属粉末和 C/C 复合材料放置石墨坩埚中，借助 RMI 工艺在 2100 ℃制备不同比例 C/C-(Hf, Zr, Ti)C，并研究了其等离子烧蚀性能。Long 等[144]以 Hf、Zr 和 Ti 金属粉末提供阳离子源，采用接触反应耦合实验研究了在 RMI 中 Hf-Zr-Ti 体系中多组分碳化物的生长行为(流程如图 18 所示)，通过表征接触反应界面的结构演变，分析了 C/C-(Hf, Zr, Ti)C 的形成过程。此外，Xu 等[145]不仅借助 RMI 工艺采用 Hf、Zr 和 Ti 金属粉末制备了 C/C-$(Hf_{0.5}Zr_{0.3}Ti_{0.2})C$，还采用新型$(Hf_{0.5}Zr_{0.3}Ti_{0.2})_2Cu$ 粉末将 C/C-WC 复合材料制备成 C/C-$(Hf_{0.5}Zr_{0.3}Ti_{0.2})C$-W-Cu 复合材料。W 和 Cu 的添加促使弯曲强度、断裂韧性和导热性分别提高了 70%、110%和 106%。此外由于 Cu、CuO 和 $WO_3$ 的“发汗效应”以及致密氧化层的形成，在烧蚀过程中会发生主动和被动保护，从而提高了 C/C-$(Hf_{0.5}Zr_{0.3}Ti_{0.2})C$-W-Cu 复合材料的抗烧蚀性能。

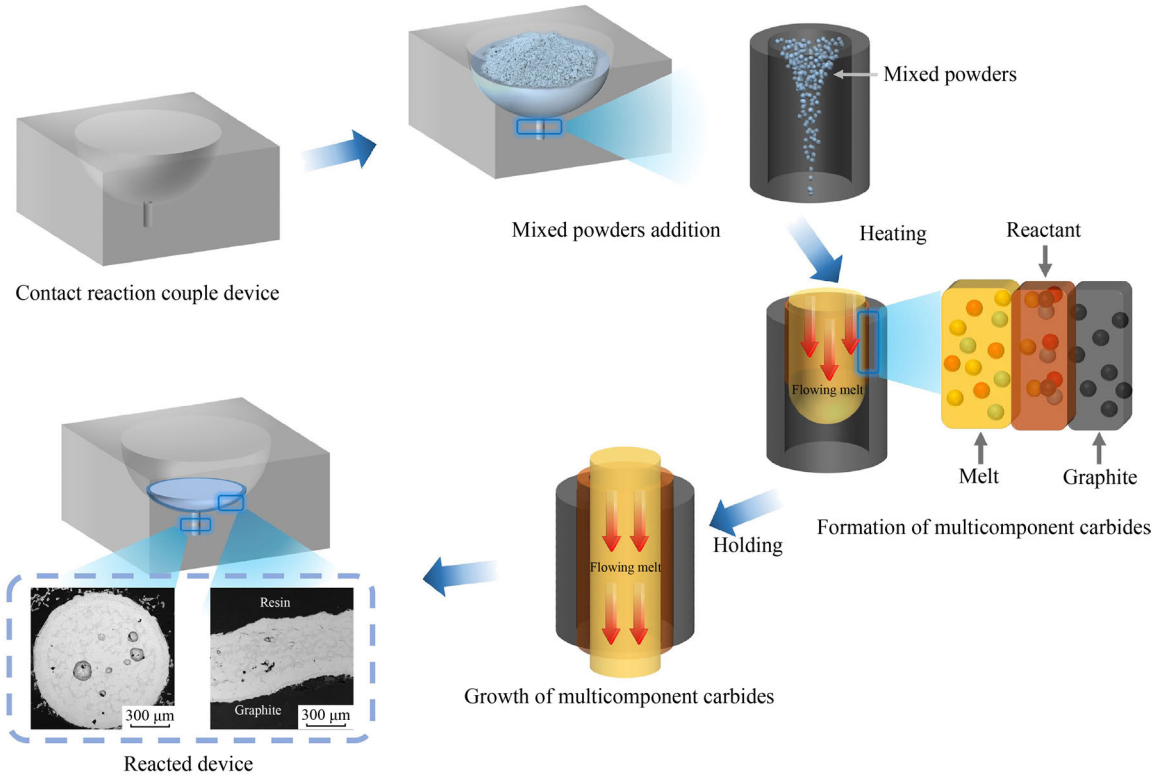



图 18 接触反应耦合设计原理示意图[144]

Fig. 18 Schematic depicting the design principle of contact reaction couple[144]

Guo 等[146]以 TiZrHfNbTa 高熵合金作为阳离子源，借助 RMI 制备了 $C_f$/(TiZrHfNbTa)C 复合材料，制备过程主要包括熔体润湿碳表面(图 19a)、熔体在毛细管力作用下渗透孔隙(图 19b)、碳原子和金属原子相互固溶并形成 HEC 陶瓷相(图 19c)及形成 $C_f$/(TiZrHfNbTa)C 复合材料(图 19d)。He 等[147]也采用相同工艺制备了致密的 $C_f$/(TiZrHfNbTa)C 复合材料，高强度和强韧性的 HEC 相的成功引入以及 $C_f$ 增强，使得该复合材料表现出优异的力学性能和抗烧蚀性能。

3) 为提高前驱体浸渍效率，缩短制备周期，Cai 等[148]还发展出浆料涂覆层压法(SIL)辅助 PIP 工艺，成功制备 2D $C_f$/$(Ti_{0.2}Zr_{0.2}Hf_{0.2}Nb_{0.2}Ta_{0.2})C$-SiC 复合材料(流程如图 20 所示)。首先于 1900 ℃热处理均匀混合的 HfC-ZrC-TaC-TiC-NbC 复相粉体合成 $(Ti_{0.2}Zr_{0.2}Hf_{0.2}Nb_{0.2}Ta_{0.2})C$ 粉体，然后将其与酚醛树脂、聚乙烯醇缩丁醛和乙醇混合均匀制得 $(Ti_{0.2}Zr_{0.2}Hf_{0.2}Nb_{0.2}Ta_{0.2})C$ 前驱体，再将 2D 纤维布置于 HEC 浆料中，在 900 ℃进行多层压制浸渍与 HEC 前驱体裂解，随后置于聚碳硅烷前驱体中并于 1100 ℃裂解，多次循环制得 2D $C_f$/$(Ti_{0.2}Zr_{0.2}Hf_{0.2}Nb_{0.2}Ta_{0.2})C$-SiC 复合材料，所制得复合材料具有优异的力学性能

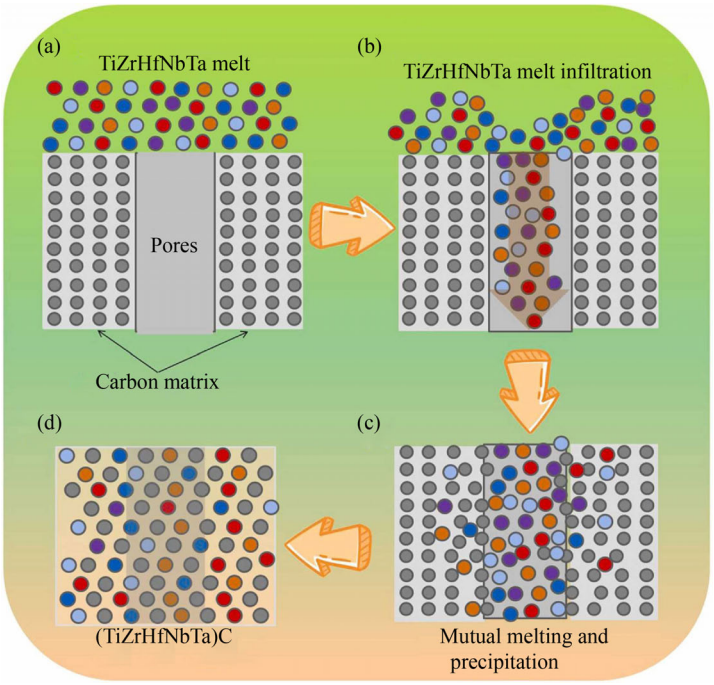



图 19　$C_f$/(TiZrHfNbTa)C 复合材料制备机理：(a)熔体润湿碳表面，(b)毛细作用促进熔体渗透，(c)碳和金属原子相互扩散并形成陶瓷相(d)(TiZrHfNbTa)C 高熵陶瓷形成[146]

Fig. 19　Preparation mechanism of $C_f$/(TiZrHfNbTa)C composites: (a) melt wets carbon surface, (b) melt infiltrates under the action of a capillary force, (c) carbon atoms and metal atoms fuse with each other and precipitate ceramic phases, and (d) (TiZrHfNbTa)C high-entropy ceramic matrix formation[146]

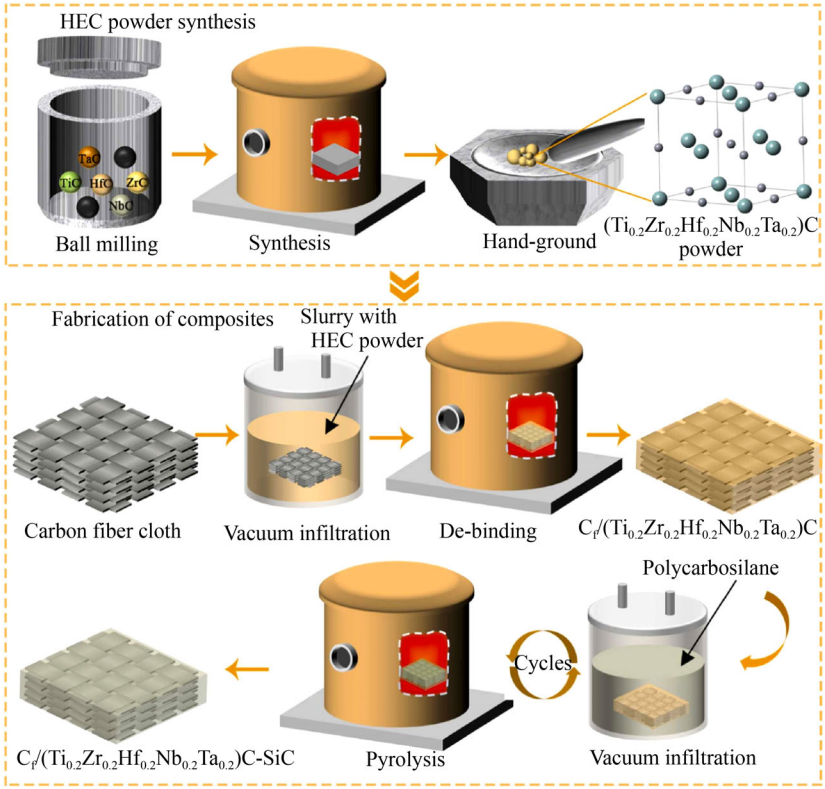



图 20　2D $C_f/(Ti_{0.2}Zr_{0.2}Hf_{0.2}Nb_{0.2}Ta_{0.2})C$-SiC 复合材料制备工艺示意图[148]

Fig. 20　Fabrication schematic of 2D $C_f/(Ti_{0.2}Zr_{0.2}Hf_{0.2}Nb_{0.2}Ta_{0.2})C$-SiC composites[148]

和抗烧蚀性能。SIL 结合 PIP 工艺也被用于制备 $C_f$/BNi/$(Ti_{0.2}Zr_{0.2}Hf_{0.2}Nb_{0.2}Ta_{0.2})C$-SiC[149]、Cf@BN/(CrZrHfNbTa)C-SiC[150]和 $C_f$/(CrZrHfNbTa)C-SiC 复合材料[151−152]。SIL 工艺需要将 HEC 粉料分散于

溶剂中，并加入一定黏结剂与分散剂配置形成均匀稳定的料浆悬浮液，利用热浸渍将料浆渗透至纤维预制件中，该方法成本低、工艺简单、涂层成分及厚度可设计性强、不受 C/C 复合材料尺寸形状限制等，但 HEC 颗粒的团聚会堵塞预制件外层的孔隙，导致后续致密化难以连续进行。

4) 除上述常见制备方法外，熔盐渗透(MSI)工艺为制备 C/C-M/HEC 提供了新途径，熔盐熔点比 Me-Si 合金熔点低 400~600 ℃，因此相较 RMI 工艺而言，MSI 工艺可显著降低渗透温度，从而削弱对 $C_f$ 的损伤[153, 154]。然而，熔盐可能与部分基体材料发生副反应，影响 C/C-M/HEC 的结构完整性和性能稳定性，因此在设计熔盐体系和工艺条件时，需综合考虑其热力学稳定性、化学兼容性及后续清洗难度等因素。

Guo 等[155]以 $K_2ZrF_6$-$K_2TiF_6$-Hf-NaCl-KCl 为原料，借助 MSI 在 900 ℃成功制备 10 种不同比例 C/C-($Ti_xZr_yHf_z$)C，(TiZrHf)C 层约为 20 μm，Ti、Zr 和 Hf 的均匀分布表现出典型的中熵陶瓷特征。Hf 分别将 $K_2ZrF_6$ 和 $K_2TiF_6$ 中 $Zr^{4+}$和 $Ti^{4+}$还原为 $Zr^{2+}$和 $Ti^{2+}$，Hf 则被氧化为 $Hf^{2+}$，随后二价金属离子发生歧化反应，产生高活性的 $Hf^*$、$Zr^*$和 $Ti^*$，并与碳反应形成($Ti_xZr_yHf_z$)C。本团队 Dong 等[154]以 NaCl、KCl、$WO_3$ 和 Cu 粉为原料，在 1300 ℃制备了 C/C-W-Cu 复合材料(图 21)。热处理过程中，盐因其具有低熔点而优先熔化，$WO_3$ 在熔融盐中溶解和扩散形成高活性的 $WO_xCl_y$，并与碳基体反应形成可与 Cu 具有良好润湿性的 W 界面层，随后熔融 Cu 在重力和毛细管力的作用下渗透到多孔基体中，填充残余孔隙。

### 3.2 涂层制备方法

目前 M/HEC 涂层制备方法主要以等离子喷涂工艺为主，本团队依托自主搭建的超音速大气等离子喷涂设备(SAPS，如图 22[156]所示)在 C/C 复合材料表面制备了(Hf-Zr-Ti)C[114, 115, 157]、(Hf-Zr-Ta)C[158]、(Hf-Zr-Nb)C[159]、(Hf-Zr-Ta-Ti)C[113]、(Hf-Zr-Ta-Nb)C[159]以及(Hf-Zr-Ti-Sc-Y-La)$C_{1-\delta}$[160]等系列 M/HEC 涂层(M/HEC-C/C)。SAPS 工艺制备 M/HEC-C/C 流程如图 23a[157]所示，首先需要借助包埋固渗工艺制备 SiC 过渡层，缓解因 C/C 基材与 M/HEC 涂层较大热失配所造成的涂层脱落，然后将 M/HEC 粉体造粒并送至等离子喷枪内，借助离子电弧将粉末加热至熔融或半熔融状态，使粉末在高速焰流推动下喷射至基材表面，经过高速冲击、变形和冷却凝固后形成涂层结构(图 23b)[115, 157]。该方法具有可设计性强、效率高等优点，但涂层存在轻微氧化以及少量孔隙，各涂层间的结合仍为机械结合。

此外，研究人员还采用化学气相沉积(CVD)工艺探索了二元固溶体及纳米线[161–174]。CVD 是一种借助前驱体气体($H_2$、$CH_4$、$ZrCl_4$、$HfCl_4$、$NbCl_5$和 $TaCl_5$ 等)在还原性气氛中反应，从而在 C/C 复合材料表面制备陶瓷涂层的方法。本团队 Zhang 等[161]综述了 CVD 工艺制备 C/C 复合材料表面硅基陶瓷涂层和超高温陶瓷涂层(碳化物、硼化物和部分氮化物)的最新进展，并详细介绍其制备工艺和抗烧蚀性能。制备流程如图 24[161]所示，主要包括以下步骤：1) 输送前驱体气体至反应室；2) 高温气相反应形成气相中间产物；3) 气相中间产物附着于基材表面，发生非均相反应，产生沉积物和副产物；4) 沉积物沿基材表面扩散，陶瓷晶粒形核；5) 去除气态副产物；6) 去除未反应前驱体气体和副产物。

CVD 工艺具有制备温度较低、不损伤 C/C 复合材料基体、涂层表面平整致密以及涂层厚度、纯度及晶型可调控等多种优势，然而受制备工艺及成分调控等因素制约，目前 CVD 所制备成分主要集中在单相及复相梯度结构涂层，然而目前有关 CVD 制备 M/HEC 陶瓷涂层报道较少[162–170]。

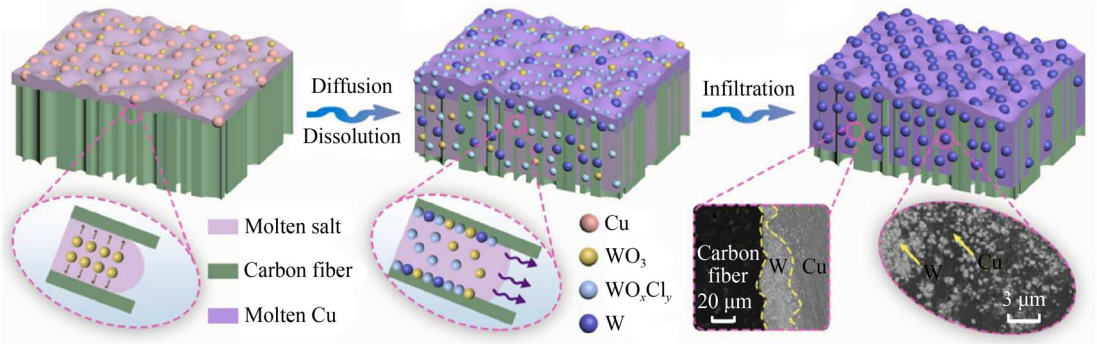



图 21 C/C-W-Cu 复合材料熔盐渗透机理示意图[154]

Fig. 21 Schematic of molten salt infiltration mechanism for C/C-W-Cu composites[154]

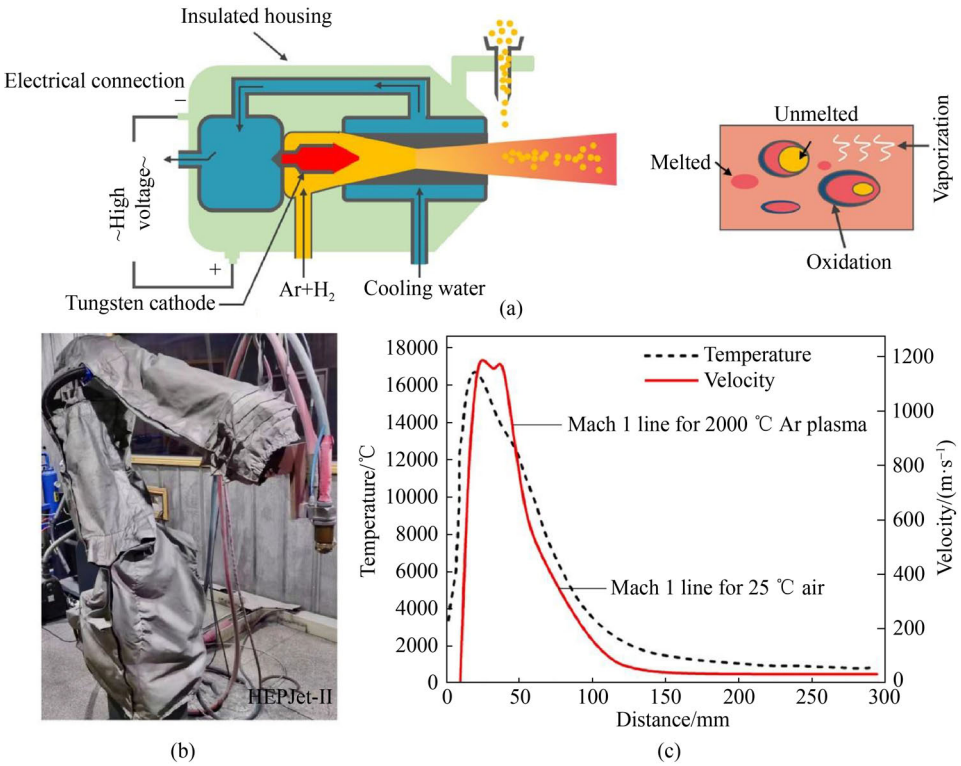



图 22　(a)空气等离子火焰中粉末结构演变示意图；(b)所采用的 SAPS 装置(HEPJet II)；(c)超音速等离子体射流的计算温度场和速度场[156]

Fig. 22　(a) Schematic diagram of structural evolution of powder in the air plasma flame; (b) the employed SAPS device (HEPJet-II); (c) the calculated temperature and velocity fields for the supersonic plasma jet[156]

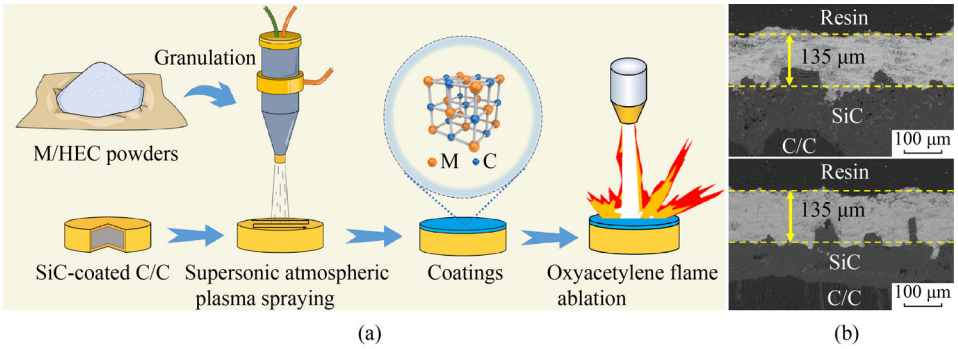



图 23　(a) M/HEC 涂层制备示意图[115]；(b) M/HEC-C/C 的截面形貌[157]

Fig. 23　(a) The schematic diagram of the preparation of M/HEC coating[115]; (b) cross-sectional morphologies of M/HEC-C/C[157]

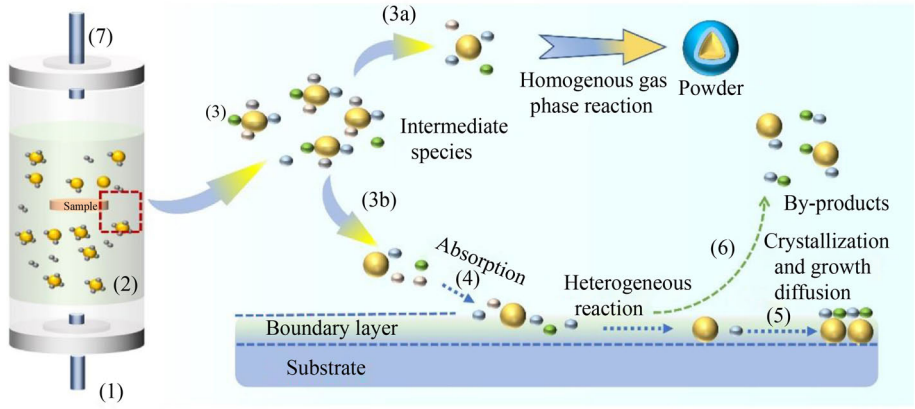



图 24　超高温陶瓷涂层 CVD 制备示意图[161]

Fig. 24　Schematic of the CVD preparation of ultra-high temperature ceramic coating[161]

本团队 Chen 等[171–174]借助 CVD 开发了一种新型 $Hf_xTa_{1-x}C$ 纳米线，阐明了其高温环境下的形貌演变规律，并基于此构建了 $Hf_xTa_{1-x}C$ 纳米线增韧超高温陶瓷涂层(图 25[171])，$Hf_xTa_{1-x}C$ 纳米线的成功制备为后续 CVD 制备 M/HEC 陶瓷涂层奠定了理论基础和技术支撑。

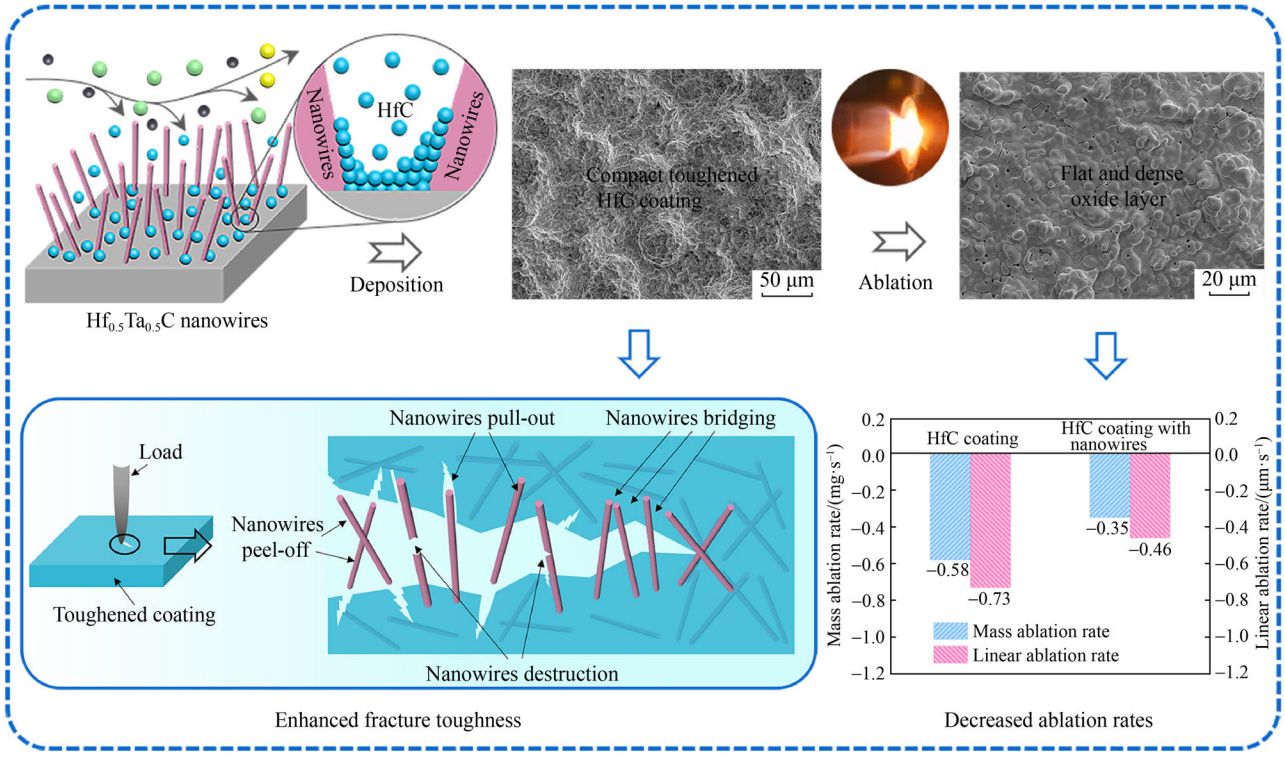



图 25 $Hf_{0.5}Ta_{0.5}C$ 固溶体纳米线增韧 HfC 涂层的微观结构、增韧机理和烧蚀性能[171]

Fig. 25 Microstructure, toughening mechanism and ablation resistance of $Hf_{0.5}Ta_{0.5}C$ solid solution nanowire-toughened HfC coating[171]

## 4 中/高熵碳化物陶瓷改性 C/C 复合材料的抗烧蚀性能

获得具有优异抗烧蚀性能的 M/HEC 基体/涂层改性 C/C 复合材料的关键在于自生氧化膜的阻氧性、高温稳定性和自愈合性，本团队系统研究了 Hf、Zr、Ta、Ti 和 Nb 元素对 M/HEC 抗烧蚀性能影响规律，结合多尺度模拟阐明了多组元协同阻氧作用机理、低熔点自愈合效应及烧蚀防护机理。不同 M/HEC-C/C 在 2.4 MW/m² 热通量下的氧乙炔烧蚀抗性比较如表 1 所示。

(Hf-Zr-Ti)C[114, 115]：$(Hf_{1/3}Zr_{1/3}Ti_{1/3})C$ 涂层烧蚀后，涂层表面形成由氧化物纳米颗粒和无定形碳氧化物组成的致密保护层(图 26a[115])，这为氧的向内扩散提供了有效的扩散屏障，这种独特结构提高了 $(Hf_{1/3}Zr_{1/3}Ti_{1/3})C$ 涂层的防护效果(图 26b)。$(Hf_{0.25}Zr_{0.25}Ti_{0.5})C$ 涂层烧蚀初期，O 原子与 Hf/Zr 原子同时反应，形成富含 Hf/Zr 的氧化物$(Hf, Zr)O_2$，

**表 1 不同 M/HEC-C/C 在 2.4 MW/m² 热通量下的氧乙炔烧蚀抗性比较**

**Table 1 Comparison of oxyacetylene ablation resistance of different M/HEC-C/C at a heat flux of 2.4 MW/m²**

| Type | Ablation time/s | Linear ablation rate/(μm·s⁻¹) | Mass ablation rate/(mg·s⁻¹) | Reference |
|---|---|---|---|---|
| $(Hf_{0.25}Zr_{0.25}Ti_{0.5})C$ | 120 | 0.67 | –0.82 | [114] |
| $(Hf_{1/3}Zr_{1/3}Ti_{1/3})C$ | 210 | –0.19 | –0.15 | [115] |
| $(Hf_{4/7}Zr_{2/7}Ta_{1/7})C$ | 90 | –0.67 | –0.38 | [141] |
| $(Hf_{4/7}Zr_{2/7}Ta_{1/7})C$-SiC | 90 | 0.07 | –0.33 | [142] |
| $(Hf_{1/3}Zr_{1/3}Ta_{1/3})C$ | 120 | 0.61 | | [158] |
| $(Hf_{1/4}Zr_{1/4}Ta_{1/4}Ti_{1/4})C$ | 180 | 0.19 | 0.81 | [113] |
| $(Hf_{0.45}Zr_{0.45}Nb_{0.1})C$ | 300 | –0.01 | –0.04 | [159] |
| $(Hf_{0.2}Zr_{0.7}Nb_{0.1})C$ | 300 | –0.09 | 0.18 | [159] |
| $(Hf_{0.7}Zr_{0.2}Nb_{0.1})C$ | 300 | 0.30 | 0.61 | [159] |

随后 $TiO_2$ 向其扩散。随着更多的 $TiO_2$ 扩散到$(Hf, Zr)O_2$ 中，氧化物发生从贫 Ti 相到富 Ti 相的转变，分别对应于 Ti 掺杂$(Hf, Zr)O_2$ 和$(Hf, Zr)TiO_4$。Ti 掺杂$(Hf, Zr)O_2$ 为氧化物骨架，可钉扎$(Hf, Zr)TiO_4$ 以避免机

械剥蚀而损坏。少量的(Hf, Zr)$TiO_4$ 修复烧蚀缺陷(裂纹和孔隙)，但大量的(Hf, Zr)$TiO_4$ 易被机械剥蚀破坏，烧蚀缺陷极易出现在(Hf, Zr)$O_2$ 和(Hf, Zr)$TiO_4$ 之间的相界面以及不同(Hf, Zr)$TiO_4$ 晶界处(图 27[114])。

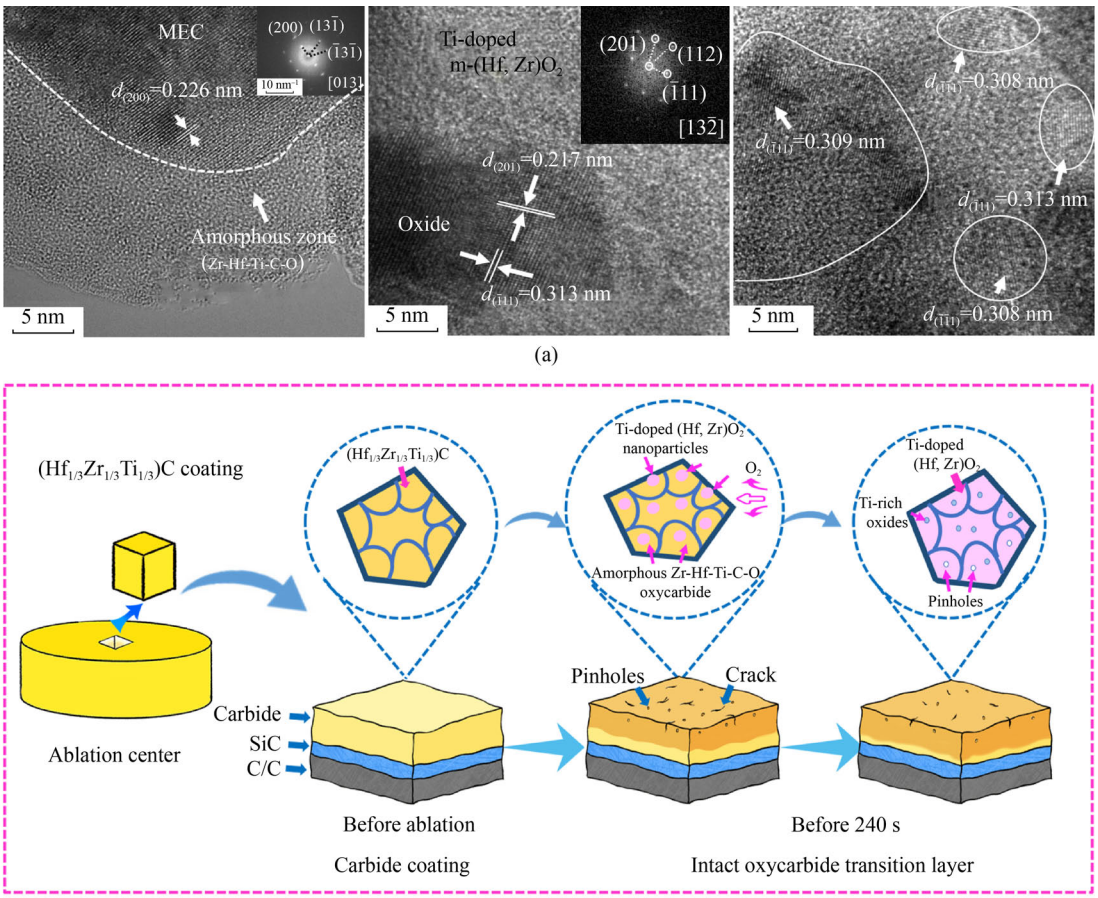



图 26　($Hf_{1/3}Zr_{1/3}Ti_{1/3}$)C-C/烧蚀后(a)TEM 图像及(b)机理示意图[115]

Fig. 26　(a) TEM images and (b) schematic of the ($Hf_{1/3}Zr_{1/3}Ti_{1/3}$)C-C/C after ablation[115]

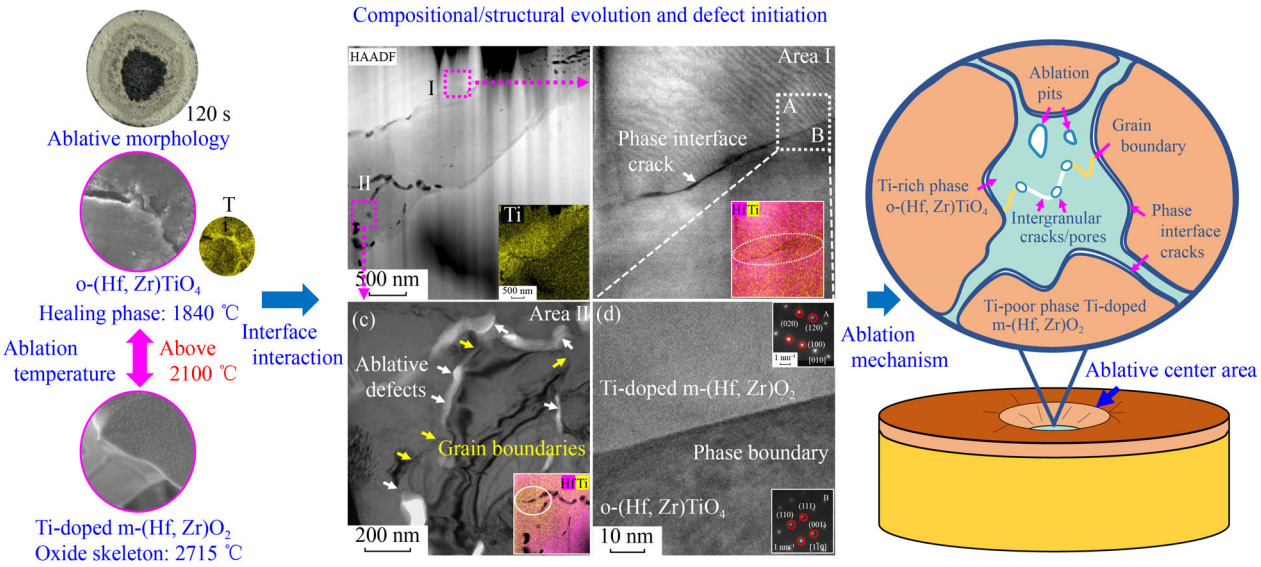



图 27　($Hf_{0.25}Zr_{0.25}Ti_{0.5}$)C-C/C 的烧蚀形貌和机理示意图[114]

Fig. 27　Ablation morphologies and mechanism schematic of ($Hf_{0.25}Zr_{0.25}Ti_{0.5}$)C-C/C[114]

(Hf-Zr-Ta)C[141, 142, 158]：Hf 和 Zr 优先氧化并固溶形成(Hf, Zr)$O_2$，这是因为 $HfO_2$ 和 $ZrO_2$ 在高温下具有相同的晶体结构(四方)，且 $Hf^{4+}$ (0.71 Å)和 $Zr^{4+}$ (0.72 Å)具有相似的离子半径。而 Ta 的氧化程度滞后，

导致氧化层下方出现富 Ta 区域(图 28a[158])，富 Ta 氧化物逐渐与(Hf, Zr)$O_2$ 反应形成 Ta 掺杂(Hf, Zr)$O_2$，随 Ta 含量增加，氧化物转变为(Hf, Zr)$_6Ta_2O_{17}$。这归因于(Hf, Zr)$_6Ta_2O_{17}$ 在~2100 ℃发生可逆包晶转变为(Hf, Zr)$O_2$ 和富 Ta 氧化物熔体[38]。高熔点氧化物骨架[Ta 掺杂(Hf, Zr)$O_2$ 和(Hf, Zr)$O_2$]和低熔点液相[$Ta_2O_5$ 和(Hf, Zr)$_6Ta_2O_{17}$]的比例对于形成结构致密性能稳定的 Hf-Zr-Ta-O 复合氧化膜至关重要。高熔点氧化物骨架具有良好的高温稳定性，能有效抵抗氧乙炔火焰侵蚀，可钉扎低熔点液相，少量氧化物熔体则通过填充骨架和液相烧结机制促进氧化层致密化，从而愈合烧蚀缺陷(图 28b)。但随着烧蚀时间的延长，氧化层中生成的 $Ta_2O_5$ 增多，并且 $Ta_2O_5$ 在烧蚀过程中以氧化物熔体的形式存在，其含量增加导致氧化层黏度的降低，此时大量低熔点液相的存在极易被机械剥蚀而形成大尺寸孔洞，破坏了氧化膜完整性。

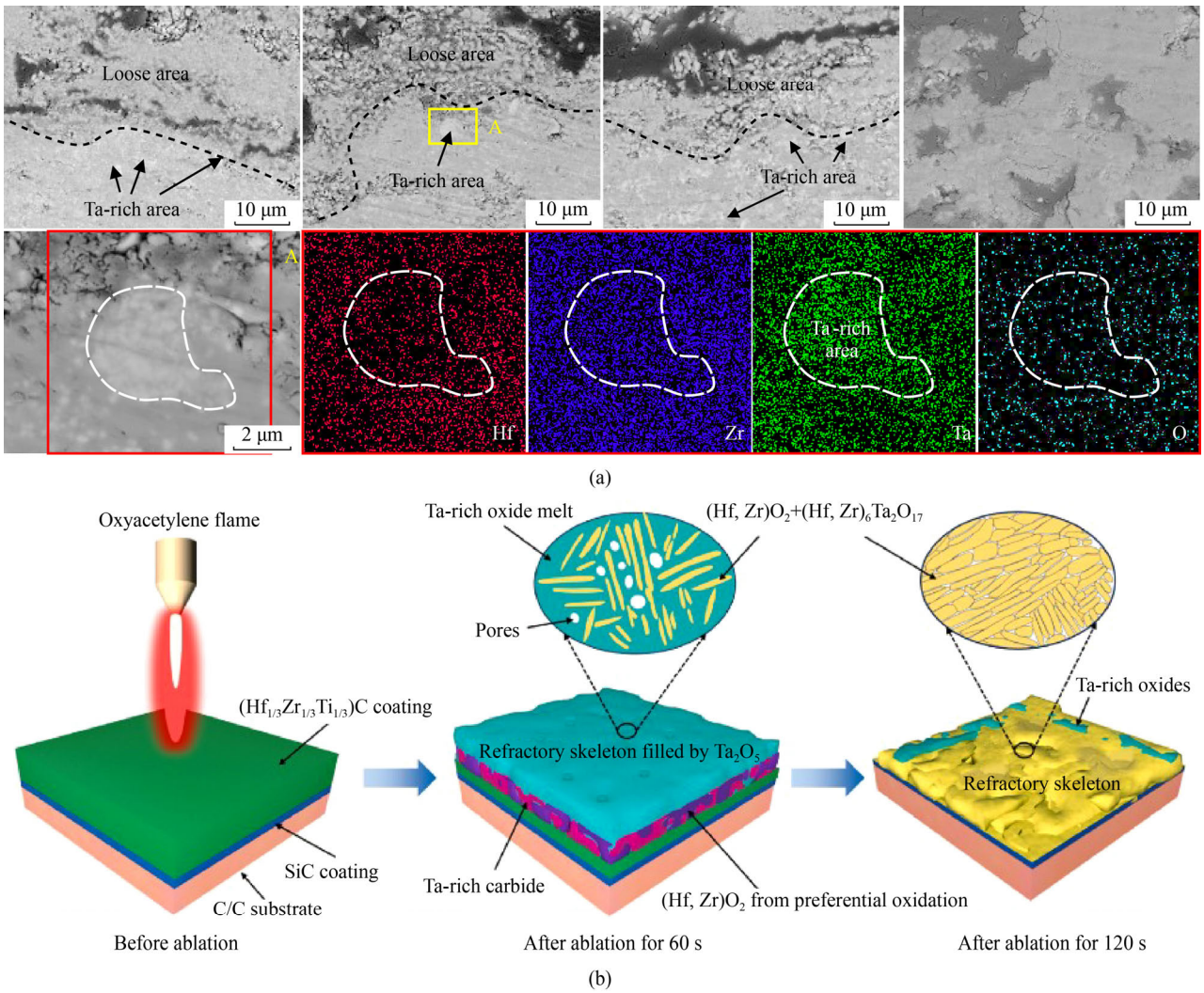



图 28 (Hf$_{1/3}$Zr$_{1/3}$Ta$_{1/3}$)C-C/C 烧蚀后(a)形貌和(b)机理示意图[158]

Fig. 28 (a) Morphologies and (b) schematic of the (Hf$_{1/3}$Zr$_{1/3}$Ta$_{1/3}$)C-C/C after ablation[158]

(Hf-Zr-Ta-Ti)C[113]：(Hf-Zr-Ta-Ti)C 构型存在 9 个不同的氧吸附位点(图 29a~图 29c)，但最终结果表明，只有 3 种稳定的构型存在，对应于 Hf-Ta-Ti-H (–5.60 eV，图 29d)、Zr-Ta-Ti-H (–5.57 eV，图 29e)和 Hf-Zr-Ta-H (–5.90 eV，图 29f)。由于 Hf-Zr-Ta-H 构型在 3 种构型中具有最低的吸附能，因此它是最稳定的 O 原子吸附构型。通过计算 Hf-Zr-Ta-H 构型的键长，发现氧吸附后，Hf—O、Zr—O、Ta—O 和 Ti—O 的键长差异率分别为 2.12%、2.64%、8.43%和 89.46%。氧化顺序为 Hf≥Zr>Ta>Ti。因此，在(Hf-Zr-Ta-Ti)C 的初始氧化过程中，O 原子优先与 Hf/Zr 原子结合，随后 Ta/Ti 原子逐渐扩散到富 Hf 的氧化物中，并产生了从 Ta/Ti 掺杂(Hf, Zr)$O_2$ 到(Hf, Zr)$_6Ta_2O_{17}$/(Hf, Zr)$TiO_4$ 的相变。

TEM 元素图谱显示 Ta 和 Ti 元素存在明显偏聚，存在 4 个不同区域(图 30a 和图 30b)。区域I上方区域 A 为 Ta/Ti 掺杂 m-(Hf, Zr)$O_2$ (图 30c)，这是由于烧蚀过程中涂层表面 Ta 和 Ti 元素的损失，并且 $TiO_2$ 比 $Ta_2O_5$ 更易挥发，因此 $TiO_2$ 和 $Ta_2O_5$ 扩散到 m-(Hf, Zr)$O_2$ 中形成 Ta 含量高于 Ti 的 Ta/Ti 掺杂(Hf, Zr)$O_2$，并未改变 m-(Hf, Zr)$O_2$ 的晶体结构。而 B 区相对于 A 区，Ta 的损失更少，大量的 $Ta_2O_5$ 可与(Hf, Zr)$O_2$ 固溶形成(Hf, Zr)$_6Ta_2O_{17}$，其晶体结构为正交结构。而不完全溶解的 $Ta_2O_5$ 导致区域 B 存在应变集中(图 30d 和图 30e)，这解释了过量的 $Ta_2O_5$ 破坏了涂层的稳定性，并且在烧蚀过程中容易被机械剥蚀破坏。然而，区域II中明暗交替的条纹以及 Ta 和 Ti 元素分布表面 *C* 和 *D* 区域存在相分离(图 30f)。SAED 揭示了沿[100]晶带轴的 o-(Hf, Zr)$TiO_4$ (区域 *C*)和 o-(Hf, Zr)$_6Ta_2O_{17}$ (区域 *D*)的纳米孪晶结构。在烧蚀开始时，O 原子首先与 Hf 和 Zr 元素反应，形成圆形的 m-(Hf, Zr)$O_2$，$TiO_2$ 的固溶在不改变 m-(Hf, Zr)$O_2$ 形状的情况下产生了 o-(Hf, Zr)$TiO_4$，而 $Ta_2O_5$ 的固溶则产生了针状超结构 o-(Hf, Zr)$_6Ta_2O_{17}$。两者交替生长，通过多层超晶格结构形成了共格纳米孪晶，减轻了它们之间晶格失配引起的应力。几何相位分析(GPA)表明应变主要集中在晶粒内部(图 30g)。纳米孪晶结构的形成增强了涂层氧化膜的韧性，提高了耐烧蚀性。

(Hf-Zr-Nb)C[159]和(Hf-Zr-Ta-Nb)C[159]：采用第一性原理计算和实验分析相结合的方法来进行优化设计(图 31a)，通过改变 Ta、Nb 元素含量以评估其对氧化层结构稳定性影响，优化元素种类及比例，可实现非等摩尔比(Hf-Zr-Ta-Nb)C 涂层抗烧蚀性能的有效提升。体系中高熔点(Hf/Zr 基氧化物)和低熔点相(Ta/Nb 基氧化物)的含量比接近 1:1 时，很难在 2000 ℃以上提供长期有效的保护(图 31b)。当固定体系 Hf/Zr 元素含量时，体系中 Ta 或 Nb 相对含量的下降可有效提高抗烧蚀性能，这归因于更多保留的 Ta/Nb 掺杂(Hf, Zr)$O_2$ 氧化物骨架对涂层结构的支撑作用，少量 Nb 元素的固溶既可以促进(Hf, Zr)$O_2$ 氧化层烧结致密，又不会引起氧化层结构变形。当固定 Nb 元素含量(摩尔分数)为 10%时，随 Zr 元素含量降低，氧化层中残留 $A_6B_2O_{17}$ 相含量增加，涂层表面氧化层中孔洞缺陷随着 Zr 元素含量降低呈先减少后增加趋势。

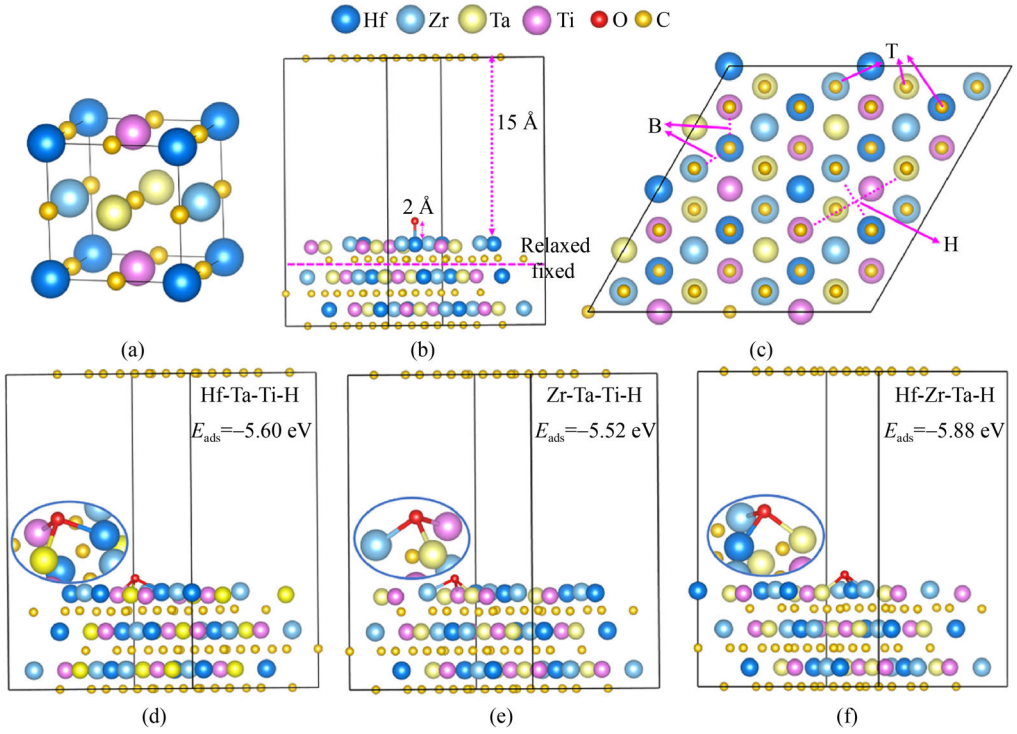



图 29　(a) HEC 单胞的结构模型；(b) HEC (111)面的侧视图和(c)俯视图；O 原子潜在吸附位点；(d~f)优化后的不同计算吸附构型：(d) Hf-Ta-Ti-H，(e) Zr-Ta-Ti-H 和(f) Hf-Zr-Ta-H[113]

Fig. 29　(a) Structural model of HEC unit cell; (b) side view and (c) top view of HEC (111) surface with possible O atom adsorption sites; (d–f) different calculated adsorption configurations after optimization: (d) Hf-Ta-Ti-H, (e) Zr-Ta-Ti-H and (f) Hf-Zr-Ta-H[113]

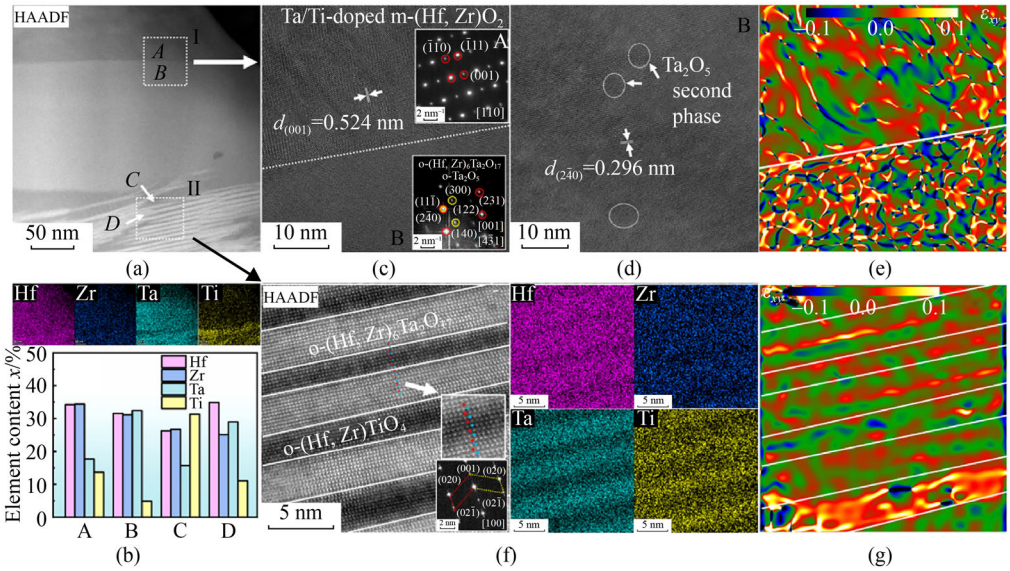



图 30 (Hf-Zr-Ta-Ti)C-C/C 烧蚀后(a) FIB 样品的 HAADF 图像，(b) *A–D* 区域的 EDS 结果，方框 I 的(c) HRTEM、(d) SAED 和(e) GPA 图像和方框 II 的(f) HAADF、元素图谱、SAED 及(g)GPA 图像[113]

Fig. 30 The (a) t HAADF image of the FIB sample, (b) EDS results of areas *A–D*, (c) the HRTEM, (d) SAED and (e) GPA images of box I and (d) the HAADF, element mapping, SAED and (g) GPA images of box II of (Hf-Zr-Ta-Ti)C-C/C after ablation[113]

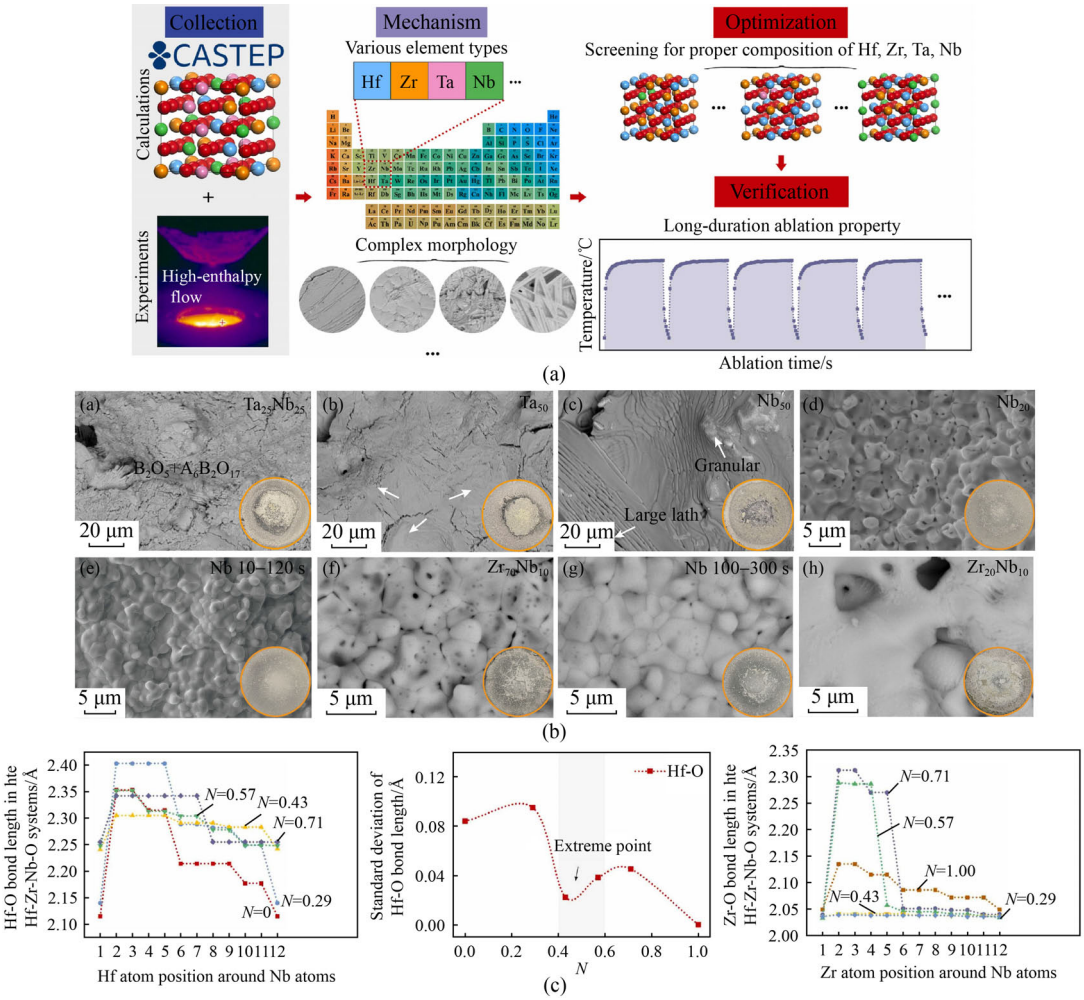



图 31 (a) (Hf-Zr-Ta-Nb)C-C/C 元素组成烧蚀性能优化设计流程图；(b)所有烧蚀样品的 SEM 图像(插图对应于烧蚀后的光学图像)；(c) Hf-Zr-Nb-O 三元系键长与 N 值关系[159]

Fig. 31 (a) Flowchart for optimization design on element-composition-ablation property of (Hf-Zr-Ta-Nb)C-C/C; (b) SEM images of all the ablated sample (inset figures corresponding to their optical image after ablation); relationship between bond lengths of Hf-Zr-Nb-O ternary systems and N value[159]

第一性原理计算结果显示 Hf—O 和 Zr—O 的键长随着 Zr 掺杂而变化(图 31c)，当 *N* 为 0.43 时(*N* 为 Zr 占 Hf-Zr-Nb 体系中的摩尔百分比)，Hf—O 键长具有最低平均值，并且随着 N 值的增加，Hf—O 的键长标准偏差先减小后增大，极值点在 0.43 左右。另一方面，从 Zr—O 键长随 N 值变化的波动趋势可以看出，当 N 不超过 0.43 时，Zr—O 的键长保持相对稳定，当 N 超过 0.57 时，Zr—O 键长显著增加。综上 Hf 和 Zr 元素含量相近时将更有益于(Hf-Zr-Nb)C 体系中氧化膜的相对稳定，因此优化的 *N* 值应在 0.4~0.5 的范围内。第一性原理计算结合实验证实 $(Hf_{0.45}Zr_{0.45}Nb_{0.1})C$ 表现出最佳长时烧蚀性能。

## 5　总结与展望

随着未来高速飞行器对抗烧蚀 C/C 复合材料的结构和性能的要求愈加苛刻，M/HEC 基体/涂层改性 C/C 复合材料的极端耦合环境服役将面临诸多挑战，同时也是新机遇，未来研究工作的重点和难点主要有以下几个方面：

1) 高效、快速开展抗氧化/烧蚀陶瓷成分设计。传统硅化物及碳化物陶瓷改性 C/C 复合材料存在高温稳定性不足、长寿命抗烧蚀性能差及防护温区窄等问题，因此获得宽温域下具有高阻氧、高稳定性及自愈合能力的原位自生氧化膜尤为重要。随着“人工智能”+材料的快速发展以及“材料基因组计划”的提出，越来越多的材料计算方法、集成计算平台和数据库被开发，因此可借助基于“人工智能”的高通量理论计算(热力学、有限元、第一性原理计算及分子动力学)结合实验验证筛选 M/HEC 成分，加速前期 M/HEC 性能数据库的建立，优化 M/HEC 成分集群，获得具有“宽温域-高阻氧-自愈合”的 M/HEC 成分设计方案。

2) 基体/涂层一体化构建与微结构调控。C/C 复合材料与 M/HEC 的微观结构和物理化学性质的差异极易导致制备和服役过程中内应力集中，进而造成基体开裂以及层间剥离等问题，削弱改性 C/C 复合材料的结合强度与抗烧蚀性能。可通过 M/HEC 定向分区改性、M/HEC 纳米相增韧、“M/HEC-掺杂相”复相镶嵌结构以及 M/HEC 梯度涂层等手段，结合计算模拟各相界面处及梯度亚层内的应力分布特征并优化结构设计，借助多尺度异质界面调控改善 M/HEC 与 C/C 复合材料的界面结合与应力分布状态，实现结合强度、抑制裂纹扩展能力以及抗烧蚀性能同步提升。

3) 明晰热/力/介质极端耦合环境下氧化/烧蚀防护机理。传统性能考核方式中通常只分析单一因素(热、力或介质)对改性 C/C 复合材料失效行为的影响，与真实极端服役环境相差甚远。需借助实际热/力(气流及粒子冲刷等加载载荷)/介质(氧、水蒸气等)等多因素耦合的服役环境考核手段(等离子/电弧风洞等)，配套原位可视化系统监测 M/HEC 基体/涂层改性 C/C 复合材料在极端服役环境下中承受超高温氧化/烧蚀、高低温热冲击和应力梯度、强气流冲刷过程中的长寿命服役稳定性及服役行为。此外，结合多尺度理论计算与先进原位表征技术，进行全方面、多尺度、深层次理论研究，阐明 M/HEC 基体/涂层改性 C/C 复合材料的“熵”和组元比例协同效应、多相异质界面作用机制及抗烧蚀防护机理。

4) 实现大尺寸复杂构件可控制备技术，加速推动其工程化应用。目前 M/HEC 基体/涂层改性 C/C 复合材料制备工艺主要局限于实验室研究，大尺寸构件的加工制备涉及多道工序和复杂的工艺流程，这不仅对大型加工设备提出新要求，同时对大尺寸复杂构件内外 M/HEC 的均匀制备以及各工艺间的精确控制提出了新挑战。亟须开发简单高效的制备技术突破大尺寸复杂构件的工艺稳定性、成分均匀性和应力变形控制以及结构/功能一体化设计等应用瓶颈。

**参考文献**:


[1] YAN M, HU C L, LI J, et al. An unusual carbon–ceramic composite with gradients in composition and porosity delivering outstanding thermal protection performance up to 1900 ℃[J]. Adv Funct Mater, 2022, 32(36): 2204133.

[2] 张雨雷, 付艳芹, 付前刚, 等. 纳米管/线多尺度强韧化 C/C 复合材料研究现状与展望[J]. 航空材料学报, 2021, 41(3): 11–24.
ZHANG Yulei, FU Yanqin, FU Qiangang, et al. J Aeronaut Mater, 2021, 41(3): 11–24.

[3] LI J C, MA Y W, LI T, et al. Enhanced oxidation/ablation resistance of $(Hf_{0.5}Zr_{0.5})C$ over HfC-ZrC *via* high oxygen-atom storage capacity across temperatures[J]. J Eur Ceram Soc, 2025, 45(15): 117625.

[4] 李秀涛, 许小静, 屈强, 等. 碳/碳热结构复合材料技术发展与展望[C]//第十一届全国新型炭材料学术研讨会论文集. 2013: 133–140.
LI Xiutao, XU Xiaojing, QU Qiang, et al. Advancement and development trends of carbon/carbon thermal-structure composites and thermal protection system technology[C]//11th National Symposium on New Carbon Materials. 2013: 133–140.

[5] ZADOROZNY E. Space Shuttle carbon-carbon composite hot structure[C]//24th Structures, Structural Dynamics and Materials Conference. Lake Tahoe, NV. Reston, Virginia: AIAA, 1983: 913.

[6] HU D, LI X X, CHEN S L, et al. Design of long-term ablation protective $Zr_{0.92}Ta_{0.04}Si_{0.04}O_2$ coating *via* large lattice distortion and limited phase precipitation[J]. Corros Sci, 2025, 245: 112689.

[7] ZHANG X, GUO L J, LIU H M, et al. Advanced anti-ablation C/C composites: Structural design strategies and future perspective[J]. Mater Today, 2024, 80: 710–736.

[8] LIU B, SUN J, GUO L X, et al. Materials design of silicon based ceramic coatings for high temperature oxidation protection[J]. Mater Sci Eng R Rep, 2025, 163: 100936.

[9] XIANG H M, XING Y, DAI F Z, et al. High-entropy ceramics: Present status, challenges, and a look forward[J]. J Adv Ceram, 2021, 10(3): 385–441.

[10] LI X X, HU D, FU J H, et al. Insights into (Hf-Zr-Ta-Nb)C thermal protective system: Ablation behavior, morphology evolution and atomic bonding[J]. Ceram Int, 2024, 50(7): 12557–12565.

[11] LV J S, LI W, LI T, et al. Ablation behavior of high-entropy boride (Hf-Zr-Ta-Ti)$B_2$ coating fabricated *via* supersonic atmospheric plasma spraying for carbon/carbon composites[J]. Compos Part B Eng, 2024, 270: 111137.

[12] ZHANG R X, SONG Q, LI J T, et al. Study on the ablation performance of SiC-coated high thermal conductivity three-dimensional C/C composites[J]. J Eur Ceram Soc, 2024, 44(6): 3797–3808.

[13] LI T, ZHANG Y L, FU Y Q, et al. Antioxidation enhancement and siliconization mitigation for SiC coated C/C composites *via* a nano-structural SiC porous layer[J]. Corros Sci, 2022, 194: 109954.

[14] LI T, ZHANG Y L, FU Y Q, et al. Siliconization elimination for SiC coated C/C composites by a pyrolytic carbon coating and the consequent improvement of the mechanical property and oxidation resistances[J]. J Eur Ceram Soc, 2021, 41(10): 5046–5055.

[15] LI T, ZHANG Y L, LV J S. Preparing the SiC coated C/C composites with excellent mechanical and antioxidative properties using a buffer layer[J]. J Eur Ceram Soc, 2022, 42(10): 4162–4171.

[16] ZHU X F, ZHANG Y L, SU Y Y, et al. SiC-Si coating with micro-pores to protect carbon/carbon composites against oxidation[J]. J Eur Ceram Soc, 2021, 41(1): 114–120.

[17] LI H J, ZHANG Y L, FU Q G, et al. Oxidation behavior of SiC nanoparticle-SiC oxidation protective coating for carbon/carbon composites at 1773K[J]. Carbon, 2007, 45(13): 2704–2707.

[18] HU D, FU Q G, ZHOU L, et al. Self-healing improvement strategy of thermally sprayed $MoSi_2$ coating at 1773 K: From calculation to experiment[J]. Corros Sci, 2021, 189: 109599.

[19] ZHANG Y T, CHEN G H, SUN J, et al. Atomic simulation and experimental: Oxidation protective SiC coating produced by chemical vapor deposition and pack cementation for carbon/carbon composites[J]. Surf Interfaces, 2024, 46: 104170.

[20] BAI Z, CAO L Y, HUANG J F, et al. Microstructures and ablation properties of Cf/C-SiC-$MoSi_2$ composites: Influence of the SiC:$MoSi_2$ mass ratio[J]. Ceram Int, 2016, 42(16): 19296–19301.

[21] GUO L L, HU X X, TAO X, et al. Low-temperature oxidation resistance of the silica-coated $MoSi_2$ powders prepared by Sol-gel preoxidation method[J]. Ceram Int, 2020, 46(15): 23471–23478.

[22] LI F J, YU X H, SHI X W, et al. Enhancing oxidation resistance of Mo metal substrate by sputtering an $MoSi_2$(N) interlayer as diffusion barrier of $MoSi_2$(Si) surface coating[J]. Surf Coat Technol, 2023, 466: 129654.

[23] LI T, ZHANG Y L, LV J S, et al. A novel $MoSi_2$-rich coating on the SiC-Si coated C/C composites for the preparation and antioxidative properties at 1773 K and 1973 K[J]. Corros Sci, 2022, 204: 110392.

[24] ZHANG Y L, LI H J, FU Q G, et al. A Si–Mo oxidation protective coating for C/SiC coated carbon/carbon composites[J]. Carbon, 2007, 45(5): 1130–1133.

[25] ZHANG Y L, LI H J, YAO X Y, et al. Oxidation protection of C/SiC coated carbon/carbon composites with Si–Mo coating at high temperature[J]. Corros Sci, 2011, 53(6): 2075–2079.

[26] LIAO N, JI Z X, YANG Z H, et al. Improved oxidation resistance of SPS sintered $Si_2BC_3N$ ceramics with disilicides ($MoSi_2$, $HfSi_2$, $TaSi_2$) addition[J]. Ceram Int, 2020, 46(11): 18079–18088.

[27] ZHU X F, ZHANG Y L, ZHANG J, et al. A compound glass coating with micro-pores to protect SiC-coated C/C composites against oxidation at 1773 K and 1973 K[J]. Corros Sci, 2022, 195: 109983.

[28] LI T, ZHANG J H, WANG P, et al. A $CrSi_2$-SiC-Si multiphase ceramic coating for SiC coated C/C composites against oxidation at 1773 K and 1973 K[J]. Ceram Int, 2025, 51(19): 28763–28770.

[29] LI T, ZHANG J H, FU Y Q, et al. Preparation of SiC/SiC-$CrSi_2$-$ZrB_2$ bilayer coating on C/C composites by a collaborative design and its oxidation behaviors at 1773 K and 1973 K[J]. Ceram Int, 2025, 51(21): 33373–33381.

[30] ZHU X F, ZHANG Y L, LI H G, et al. SiC/SiC-$ZrSi_2$ coating with micro-pore to protect C/C composites against oxidation for long-life service at high temperatures[J]. Corros Sci, 2021, 191: 109780.

[31] ZHU X F, ZHANG Y L, ZHANG J, et al. A gradient composite coating to protect SiC-coated C/C composites against oxidation at mid and high temperature for long-life service[J]. J Eur Ceram Soc, 2021, 41(16): 123–131.

[32] LI H J, YAO X Y, ZHANG Y L, et al. Anti-oxidation properties of $ZrB_2$ modified silicon-based multilayer coating for carbon/carbon composites at high temperatures[J]. Trans Nonferrous Met Soc China, 2013, 23(7): 2094–2099.

[33] HU D, FU Q G, ZHOU L, et al. Crack development behavior in thermally sprayed anti-oxidation coating under repeated thermal-oxygen coupling environment[J]. Ceram Int, 2021, 47(11): 15328–15336.

[34] LV J S, LI W, LI Z L, et al. Ablation-resistant (Hf, Zr)$B_2$–SiC composite coating with alternating lamellar architecture by one-step atmospheric plasma spraying[J]. Compos Part B Eng, 2025, 297: 112302.

[35] REN J C, ZHANG Y L, ZHANG P F, et al. Ablation resistance of HfC coating reinforced by HfC nanowires in cyclic ablation environment[J]. J Eur Ceram Soc, 2017, 37(8): 2759–2768.

[36] NI D W, CHENG Y, ZHANG J P, et al. Advances in ultra-high temperature ceramics, composites, and coatings[J]. J Adv Ceram, 2022, 11(1): 550.

[37] LV J S, LI W, FU Y Q, et al. Functionally graded oxide scale on (Hf, Zr, Ti)$B_2$ coating with exceptional ablation resistance induced by unique Ti dissolving[J]. Adv Sci, 2025, 12(10): 2411292.

[38] LV J S, LI W, LI T, et al. Multicomponent (Hf-Zr-Ta)$B_2$ coatings for carbon/carbon composites and structural optimization enabling superior ablation resistance[J]. J Mater Sci Technol, 2025, 204: 115–126.

[39] ZHANG S, WANG X H, XIANG H M, et al. Unraveling the CMAS corrosion mechanism of $CrTaO_4$: A promising dual function oxidation and thermal protection material for RHEAs[J]. J Mater Sci Technol, 2025, 233: 80–93.

[40] ZHANG S, WANG X H, ZHANG C, et al. Microstructure, elastic/mechanical and thermal properties of $CrTaO_4$: A new thermal barrier material [J]. J Adv Ceram, 2024, 13(3): 373–387.

[41] REN J C, FENG E R, ZHANG Y L, et al. Influences of deposition temperature, gas flow rate and ZrC content on the microstructure and anti-ablation performance of CVD-HfC-ZrC coating[J]. Ceram Int, 2021, 47(1): 556–566.

[42] LU J H, HAO K, LIU L, et al. Ablation resistance of SiC–HfC–ZrC multiphase modified carbon/carbon composites[J]. Corros Sci, 2016, 103: 1–9.

[43] REN J C, FENG E R, ZHANG Y L, et al. Microstructure and anti-ablation performance of HfC-TaC and HfC-ZrC coatings synthesized by CVD on C/C composites[J]. Ceram Int, 2020, 46(8): 10147–10158.

[44] REN J C, ZHANG Y L, ZHANG J, et al. Effects of HfC nanowire amount on the microstructure and ablation resistance of CVD-HfC coating[J]. Ceram Int, 2018, 44(10): 11340–11349.

[45] ZHANG J, ZHANG Y L, FU Y Q, et al. Effect of HfC-SiC transition layer on the ablation resistance of SiC/HfC-SiC/HfC multi-layer coating for C/C composites[J]. Vacuum, 2019, 169: 108886.

[46] CHEN L, ZHANG W, TAN Y Q, et al. Influence of vanadium content on the microstructural evolution and mechanical properties of (TiZrHfVNbTa)C high-entropy carbides processed by pressureless sintering[J]. J Eur Ceram Soc, 2021, 41(16): 60–67.

[47] FU Y Q, ZHANG Y L, CHEN H, et al. Ultra-high temperature performance of carbon fiber composite reinforced by HfC nanowires: A promising lightweight composites for aerospace engineering[J]. Compos Part B Eng, 2023, 250: 110453.

[48] FU Y Q, ZHANG Y L, LI T, et al. Thermal shock resistance of carbon-based composites reinforced by HfC nanowires under extreme conditions[J]. Ceram Int, 2024, 50(19): 35287–35297.

[49] FU Y Q, ZHANG Y L, YIN X M, et al. Two birds with one stone: Simultaneous fabrication of HfC nanowires and CNTs through efficient utilization of polymer-derived ceramics[J]. J Mater Sci Technol, 2022, 129: 163–172.

[50] FU Y Q, ZHANG Y L, CHEN H, et al. Ultra-high temperature resistance of one-dimensional hafnium carbide wrapped with pyrolytic carbon up to 2450 ℃[J]. Corros Sci, 2022, 195: 110015.

[51] FU Y Q, ZHANG Y L, ZHANG J, et al. Radially one-dimensional hafnium carbide-carbon/carbon networks composites for ultra-high temperature ablation-resistance[J]. Corros Sci, 2021, 185: 109443.

[52] JIA Y J, LI H J, FU Q G, et al. Ablation resistance of supersonic-atmosphere-plasma-spraying ZrC coating doped with $ZrO_2$ for SiC-coated carbon/carbon composites[J]. Corros Sci, 2017, 123: 40–54.

[53] JIA Y J, LI H J, SUN J J, et al. Ablation resistance of SiC-modified ZrC coating prepared by SAPS for SiC-coated carbon/carbon composites[J]. Int J Appl Ceram Technol, 2017, 14(3): 331–343.

[54] LIU T Y, FU Q G, LIU B, et al. Effect of temperature gradient on the ablation and flexural behavior of C/C-ZrC composites[J]. Corros Sci, 2021, 191: 109736.

[55] ZHAO Z G, LI K Z, KOU G, et al. Comparative research on cyclic ablation behavior of C/C-ZrC-SiC and C/C-ZrC composites at temperatures above 2000 ℃[J]. Corros Sci, 2022, 206: 110496.

[56] REN J C, ZHANG Y L, FU Y Q, et al. Effects of the second phase on the microstructure and ablation resistance of HfC coating on C/C composites[J]. Surf Coat Technol, 2018, 344: 250–258.

[57] DONG Z J, YU H Z, ZHANG Y, et al. C/C-HfC-ZrC composites with excellent long-term ablation performance prepared by combining PIP and RMI[J]. Ceram Int, 2024, 50(8): 13912–13923.

[58] LI J C, LI T, HUANG C J, et al. The synergistic effect of multi-phase oxides on the ablation resistance of TaC-modified HfC-ZrC coatings for C/C composites[J]. Corros Sci, 2024, 228: 111795.

[59] ZHANG J, ZHANG Y L, FU Y Q, et al. Preparation and ablation behavior of HfC-SiC co-deposited coatings with different proportions[J]. Corros Sci, 2021, 192: 109853.

[60] ZHANG Y Y, ZHANG X M, GUO L X, et al. Effect of temperature-dependent nano SiC on the ablation resistance of ZrC coating[J]. J Eur Ceram Soc, 2024, 44(12): 6875–6888.

[61] ZHANG Y Y, SUN J, GUO L X, et al. Ablation resistant ZrC coating modified by polymer-derived SiC/TiC nanocomposites for ultra-high temperature application[J]. J Eur Ceram Soc, 2022, 42(1): 18–29.

[62] LI B, LI H J, YAO X Y, et al. Ablation behavior of $(ZrC/SiC)_3$ alternate coating prepared on sharp leading edge C/C composites by CVD[J]. J Mater Sci Technol, 2022, 115: 129–139.

[63] LIU Z Q, SUN Y F, ZHANG S B, et al. Microstructure and ablation resistance of C/C-HfC-SiC composites prepared by RMI with different powder particle sizes[J]. Mater Charact, 2024, 218: 114577.

[64] LIU Z Q, JIA Y J, HOU J Q, et al. C/C-HfC-SiC composites with simultaneous the resistance to ultra-high temperature airflow erosion and high temperature oxidation[J]. J Materiomics, 2025, 11(1): 100846.

[65] LIU Z Q, FU Q G, SHI H L, et al. Comparative study of microstructure and ablation behaviour of C/C-HfC-SiC composites prepared under two different conditions[J]. Mater Charact, 2022, 194: 112467.

[66] LIU Z Q, ZHANG S B, ZHANG J P, et al. Effect of gaseous silicon infiltration process on mechanical and ablation properties of C/C-HfC-SiC composites with $HfSi_2$/HfC coating prepared by reactive melt infiltration[J]. Compos Commun, 2025, 56: 102358.

[67] WANG R N, ZHANG J P, LIU B, et al. Ablation of advanced C/C-ZrC-SiC leading edge composites[J]. Corros Sci, 2024, 226: 111648.

[68] WANG R N, LI N, ZHANG J P, et al. Ablation behavior of sharp leading-edge C/C-ZrC-SiC composites using 3000 ℃ oxyacetylene torch[J]. Corros Sci, 2022, 206: 110551.

[69] HE R X, LI K Z, ZHANG W H, et al. Film-forming investigation of NbC-modified HfC coating based on oxyacetylene ablation and argon-atmosphere heating above 2000 ℃[J]. Corros Sci, 2023, 220: 111303.

[70] HE R X, LI K Z, GU S Y, et al. Comparing ablation properties of NbC and NbC-25 mol.% ZrC coating on SiC-coated C/C composites[J]. Ceram Int, 2020, 46(6): 7055–7064.

[71] HE R X, LI K Z, LIU L Q. Solubility, crystal growth, and film-formation mechanism of NbC-modified ZrC coating under oxyacetylene flame[J]. Appl Surf Sci, 2023, 625: 157123.

[72] FENG G H, LI H J, YANG L, et al. Investigation on the ablation performance and mechanism of HfC coating modified with TaC[J]. Corros Sci, 2020, 170: 108649.

[73] SHUAI K, ZHANG Y L, FU Y Q, et al. $MoSi_2$-HfC/TaC-HfC multi-phase coatings synthesized by supersonic atmospheric plasma spraying for C/C composites against ablation[J]. Corros Sci, 2021, 193: 109884.

[74] FENG G H, LI H J, YAO X Y, et al. Ablation resistance of HfC-TaC/HfC-SiC alternate coating for SiC-coated carbon/carbon composites under cyclic ablation[J]. J Eur Ceram Soc, 2021, 41(6):

3207–3218.

[75] HU D, FU Q G, TONG M D, et al. Multiple cyclic ablation behaviors of multilayer ZrC-TaC coating with ZrC-SiC interface layer[J]. Corros Sci, 2022, 200: 110215.

[76] HU D, ZHANG Y T, DONG Z J, et al. Relationship analyses on environmental factors-ablation performance based on ZrC-TaC system: Oxygen partial pressure and gas flow scouring[J]. J Eur Ceram Soc, 2023, 43(6): 2331–2344.

[77] HU D, FU Q G, DONG Z J, et al. Design of ablation resistant Zr-Ta-O-C composite coating for service above 2400 ℃[J]. Corros Sci, 2022, 200: 110221.

[78] HU D, FU Q G, LI X X, et al. Discussion on structural parameters of the multilayer ZrC/TaC coatings based on stress analysis and ablation behaviors[J]. Surf Coat Technol, 2022, 435: 128243.

[79] ZHANG M L, ZHANG X H, HU D, et al. Ablation resistant C/C-HfC-ZrC-TaC-SiC composites prepared by reactive melt infiltration[J]. Ceram Int, 2024, 50(20): 37820–37832.

[80] LI J C, LU F Y, FU Y Q, et al. The oxidation/ablation differences of multi-phase carbide ceramics evaluated by atomic simulations and performance data validation[J]. Compos Part B Eng, 2025, 302: 112552.

[81] LI J C, ZHANG Y L, LV J S, et al. Sealing role of Ti-rich phase in HfC-ZrC-TiC coating for C/C composites during ablation above 2100 ℃[J]. Corros Sci, 2022, 205: 110474.

[82] HAJDUK B, BEDNARSKI H, JARKA P, et al. Thermal and optical properties of PMMA films reinforced with $Nb_2O_5$ nanoparticles[J]. Sci Rep, 2021, 11(1): 22531.

[83] LIU S P, MA Z, LIU Y B, et al. Ablation performance of $Ta_{0.8}Hf_{0.2}C$-SiC coating fabricated *via* pack cementation for carbon/carbon composites[J]. J Eur Ceram Soc, 2025, 45(4): 117064.

[84] DUBE T C, ZHANG J. Underpinning the relationship between synthesis and properties of high entropy ceramics: A comprehensive review on borides, carbides and oxides[J]. J Eur Ceram Soc, 2024, 44(3): 1335–1350.

[85] YE B L, WEN T Q, NGUYEN M C, et al. First-principles study, fabrication and characterization of $(Zr_{0.25}Nb_{0.25}Ti_{0.25}V_{0.25})C$ high-entropy ceramics[J]. Acta Mater, 2019, 170: 15–23.

[86] BACKMAN L, GILD J, LUO J, et al. Part I: Theoretical predictions of preferential oxidation in refractory high entropy materials[J]. Acta Mater, 2020, 197: 20–27.

[87] ROST C M, SACHET E, BORMAN T, et al. Entropy-stabilized oxides[J]. Nat Commun, 2015, 6: 8485.

[88] WANG Y C, REECE M J. Oxidation resistance of (Hf-Ta-Zr-Nb)C high entropy carbide powders compared with the component monocarbides and binary carbide powders[J]. Scr Mater, 2021, 193: 86–90.

[89] LUN H L, ZENG Y, XIONG X, et al. Oxidation behavior of non-stoichiometric (Zr, Hf, Ti)Cx carbide solid solution powders in air[J]. J Adv Ceram, 2021, 10(4): 741–757.

[90] TAN Y Q, CHEN C, LI S G, et al. Oxidation behaviours of high-entropy transition metal carbides in 1200 ℃ water vapor[J]. J Alloys Compd, 2020, 816: 152523.

[91] GILD J, ZHANG Y Y, HARRINGTON T, et al. High-entropy metal diborides: A new class of high-entropy materials and a new type of ultrahigh temperature ceramics[J]. Sci Rep, 2016, 6: 37946.

[92] YE B L, WEN T Q, HUANG K H, et al. First-principles study, fabrication, and characterization of $(Hf_{0.2}Zr_{0.2}Ta_{0.2}Nb_{0.2}Ti_{0.2})C$ high-entropy ceramic[J]. J Am Ceram Soc, 2019, 102(7): 4344–4352.

[93] LIU S Y, ZHANG S X, LIU S Y, et al. Phase stability, mechanical properties and melting points of high-entropy quaternary metal carbides from first-principles[J]. J Eur Ceram Soc, 2021, 41(13): 6267–6274.

[94] LIU S Y, ZHANG S X, LIU S Y, et al. Stability and mechanical properties of single-phase quinary high-entropy metal carbides: First-principles theory and thermodynamics[J]. J Eur Ceram Soc, 2022, 42(7): 3089–3098.

[95] HOSSAIN M D, BORMAN T, OSES C, et al. Entropy landscaping of high-entropy carbides[J]. Adv Mater, 2021, 33(42): 2102904.

[96] SARKER P, HARRINGTON T, TOHER C, et al. High-entropy high-hardness metal carbides discovered by entropy descriptors[J]. Nat Commun, 2018, 9(1): 4980.

[97] MENG H, YU R W, TANG Z Y, et al. Formation ability descriptors for high-entropy carbides established through high-throughput methods and machine learning[J]. Cell Rep Phys Sci, 2023, 4(8): 101512.

[98] ZHANG Y B, WEI J, LI X T, et al. Sintering, toughening mechanism and amorphization of $B_4C$-based ceramic composites: A review[J]. J Eur Ceram Soc, 2025, 45(4): 117075.

[99] XIE H, QIN M D, HONG M, et al. Rapid liquid phase-assisted ultrahigh-temperature sintering of high-entropy ceramic composites[J]. Sci Adv, 2022, 8(27): eabn8241.

[100] AKRAMI S, EDALATI P, FUJI M, et al. High-entropy ceramics: Review of principles, production and applications[J]. Mater Sci Eng R Rep, 2021, 146: 100644.

[101] 蔡飞燕, 倪德伟, 董绍明. 高熵碳化物超高温陶瓷的研究进展[J]. 无机材料学报, 2024, 39(6): 591–608.
CAI Feiyan, NI Dewei, DONG Shaoming. J Inorg Mater, 2024, 39(6): 591–608.

[102] 李筱暄, 付前刚, 文子豪,等.极端环境用超高温陶瓷结构材料研究进展[J]. 无机材料学报, 2025, 40(10): 1045–1078.
LI Xiaoxuan, FU Qiangang, WEN Zihao, et al. J Inorg Mater, 2025, 40(10): 1045–1078.

[103] SONG W L, CHEN Z K, CHEN S Y, et al. A new sight on the influence of molten salt in the preparation of (Ta, Nb, Ti)C nanopowder[J]. Adv Eng Mater, 2024, 26(18): 2302157.

[104] NING S S, WEN T Q, YE B L, et al. Low-temperature molten salt synthesis of high-entropy carbide nanopowders[J]. J Am Ceram Soc, 2020, 103(3): 2244–2251.

[105] AN H B, CHEN R Y, LI S S, et al. Influence of (Ta Nb Ti V)C powders synthesized by molten salt at low temperature on densification and properties of high entropy carbide ceramics[J]. J Am Ceram Soc, 2024, 107(7): 4679–4688.

[106] MA Y Z, PAN A F, YANG X F, et al. Molten salt synthesis of highly crystalized (TaNbTiV)C flake and its electromagnetic wave absorption property[J]. Ceram Int, 2024, 50(1): 81–93.

[107] 杨宇, 陈庚, 李慧, 等. 熔盐电脱氧工艺制备纳米级(VNbTaZrHf)C高熵碳化物及其析氢反应的催化性能[J]. 稀有金属材料与工程, 2024, 53(6): 1566–1573.
YANG Yu, CHEN Geng, LI Hui, et al. Rare Met Mater Eng, 2024, 53(6): 1566–1573.

[108] LIU D, FU Q G, CHU Y H. Molten salt synthesis, formation mechanism, and oxidation behavior of nanocrystalline $HfB_2$ powders[J]. J Adv Ceram, 2020, 9(1): 35–44.

[109] LI J C, LU F Y, LI T, et al. Superior synergistic oxidation resistance of medium-entropy carbide ceramic powders rather than multi-phase carbide ceramic powders[J]. J Adv Ceram, 2024, 13(8): 1223–1233.

[110] FENG L, FAHRENHOLTZ W G, HILMAS G E. Low-temperature sintering of single-phase, high-entropy carbide ceramics[J]. J Am Ceram Soc, 2019, 102(12): 7217–7224.

[111] ZHANG J T, ZHAN Y X, REN Z K, et al. Synthesis of (WZrNbTaM)C (M=Cr, Ni, Ti) ceramic powders and the electromagnetic wave absorption in 2–18 GHz[J]. J Am Ceram Soc, 2024, 107(5): 3313–3328.

[112] ZHANG J T, WANG W L, ZHANG Z X, et al. Synthesis, microstructure, mechanical and tribological properties of high-entropy carbides (WZrNbTaTi)C-SiCw[J]. Ceram Int, 2024, 50(23): 50780–50792.

[113] LI J C, ZHAO J H, LI T, et al. Microstructure evolution and phase interface characterization in anti-ablation ($Hf_{1/4}Zr_{1/4}Ta_{1/4}Ti_{1/4}$)C-coated C/C composites[J]. Compos Part B Eng, 2024, 281: 111569.

[114] LI J C, LU F Y, LI T, et al. The interface interaction within multi-phase oxides on the ablation behavior of the ($Hf_{0.25}Zr_{0.25}Ti_{0.5}$)C-coated C/C composites[J]. Surf Coat Technol, 2024, 493: 131293.

[115] LI J C, ZHANG Y L, ZHAO Y X, et al. A novel ($Hf_{1/3}Zr_{1/3}Ti_{1/3}$)C medium-entropy carbide coating with excellent long-life ablation resistance applied above 2100 ℃[J]. Compos Part B Eng, 2023, 251: 110467.

[116] YU D, YIN J, ZHANG B H, et al. Pressureless sintering and properties of ($Hf_{0.2}Zr_{0.2}Ta_{0.2}Nb_{0.2}Ti_{0.2}$)C high-entropy ceramics: The effect of pyrolytic carbon[J]. J Eur Ceram Soc, 2021, 41(6): 3823–3831.

[117] ZHANG J T, XU S, WEN C M, et al. A study on He ion irradiation damage in ($Ti_{0.25}Zr_{0.25}Nb_{0.25}Ta_{0.25}$)C high-entropy carbide ceramics from room temperature to 700 ℃[J]. J Eur Ceram Soc, 2025, 45(1): 116855.

[118] SUN K B, YANG Z W, MU R J, et al. Densification and joining of a (HfTaZrNbTi)C high-entropy ceramic by hot pressing[J]. J Eur Ceram Soc, 2021, 41(6): 3196–3206.

[119] WANG F, ZHANG X, YAN X L, et al. The effect of submicron grain size on thermal stability and mechanical properties of high-entropy carbide ceramics[J]. J Am Ceram Soc, 2020, 103(8): 4463–4472.

[120] ZHANG Q, ZHANG J Y, LI N, et al. Understanding the electronic structure, mechanical properties, and thermodynamic stability of (TiZrHfNbTa)C combined experiments and first-principles simulation[J]. J Appl Phys, 2019, 126(2): 025101.

[121] PENG Z, SUN W, XIONG X, et al. Novel refractory high-entropy ceramics: Transition metal carbonitrides with superior ablation resistance[J]. Corros Sci, 2021, 184: 109359.

[122] CHEN Z Z, WANG H X, LI C R, et al. Oxyacetylene ablation of ($Hf_{0.2}Ti_{0.2}Zr_{0.2}Ta_{0.2}Nb_{0.2}$)C at 1350−2050 ℃[J]. J Eur Ceram Soc, 2023, 43(6): 2700–2707.

[123] ZHANG Z H, LIU Z F, LU J F, et al. The sintering mechanism in spark plasma sintering–Proof of the occurrence of spark discharge[J]. Scr Mater, 2014, 81: 56–59.

[124] LIU Y L, YI M D, LI Q, et al. Low-temperature sintering mechanization of high-entropy (W, Nb, Mo, Ta, Ti)C cermet *via* spark plasma coupled high-frequency induction sintering[J]. Ceram Int, 2024, 50(9): 14936–14947.

[125] DU B, LIU H H, CHU Y H. Fabrication and characterization of polymer-derived high-entropy carbide ceramic powders[J]. J Am Ceram Soc, 2020, 103(8): 4063–4068.

[126] SUN Y N, CHEN F H, QIU W F, et al. Synthesis of rare earth containing single-phase multicomponent metal carbides *via* liquid polymer precursor route[J]. J Am Ceram Soc, 2020, 103(11): 6081–6087.

[127] SUN Y N, YE L, ZHANG Y Q, et al. Synthesis of high entropy carbide ceramics *via* polymer precursor route[J]. Ceram Int, 2022, 48(11): 15939–15945.

[128] ZHAO J H, ZHANG Y L, CHEN H, et al. Single-source precursor derived high-entropy metal–carbide nanowires: Microstructure and growth evolution[J]. J Adv Ceram, 2023, 12(11): 2041–2052.

[129] LI X, ZHANG Y L, FU Y Q, et al. From molecular precursors to ultra-high temperature ceramics: A novel synthesis of hafnium carbonitride nanoceramics[J]. J Mater Sci Technol, 2025, 223: 11–21.

[130] CAO Z N, SUN J L, MENG L T, et al. Progress in densification and toughening of high entropy carbide ceramics[J]. J Mater Sci Technol, 2023, 161: 10–43.

[131] WANG L, CAO X X, LI Z H, et al. Synthesis and oxidation behavior of Ti-Zr-Ta(Hf) high entropy carbide nanopowders by Sol–gel method[J]. Ceram Int, 2024, 50(24): 52439–52450.

[132] ZHANG W C, GUO F W, ZHANG R J, et al. A simple route to synthesize high-entropy carbide ($Hf_{0.2}Zr_{0.2}Ti_{0.2}Ce_{0.2}La_{0.2}$)$C_{1-\delta}$ nanoparticles with large covalent radius difference[J]. Ceram Int, 2023, 49(23): 38566–38574.

[133] ZHANG X L, ZHANG W B, YIN Y, et al. Sol–gel method preparation and high-rate energy storage of high-entropy ceramic (FeCoCrMnNi)C porous powder[J]. Ceram Int, 2023, 49(17): 29327–29338.

[134] 刘泰山, 李瑞珍, 郑金煌, 等. 碳化物陶瓷改性碳/碳复合材料抗烧蚀性能研究进展[J]. 材料导报, 2024, 38(增刊 2): 103–108.
LIU Taishan, LI Ruizhen, ZHENG Jinhuang, et al. Mater Rep, 2024, 38(Suppl 2): 103–108

[135] MAKURUNJE P, MIDDLEBURGH S C, LEE W E. Addressing high processing temperatures in reactive melt infiltration for multiphase ceramic composites[J]. J Eur Ceram Soc, 2023, 43(2): 183–197.

[136] SONG X, ZHANG Z W, YE L, et al. Preparation and ablation behavior analysis of non-equimolar Cf/($Hf_{1/2}Zr_{1/3}Ti_{1/6}$)C composites under oxyacetylene flame with different heat fluxes[J]. Ceram Int, 2024, 50(15): 26482–26492.

[137] MIAO H M, XIE C Y, WANG Y F, et al. Fabrication and properties of 3-dimensional 5-directional Cf/($Zr_{0.2}Hf_{0.2}Ta_{0.2}Nb_{0.2}Ti_{0.2}$)C-SiC high-entropy ceramic matrix composites by precursor infiltration and pyrolysis process[J]. Ceram Int, 2025, 51(11): 15055–15066.

[138] CAI F Y, NI D W, CHEN B W, et al. Fabrication and properties of Cf/($Ti_{0.2}Zr_{0.2}Hf_{0.2}Nb_{0.2}Ta_{0.2}$)C-SiC high-entropy ceramic matrix composites *via* precursor infiltration and pyrolysis[J]. J Eur Ceram Soc, 2021, 41(12): 5863–5871.

[139] CAI F Y, NI D W, BAO W C, et al. Ablation behavior and mechanisms of Cf/($Ti_{0.2}Zr_{0.2}Hf_{0.2}Nb_{0.2}Ta_{0.2}$)C–SiC high-entropy ceramic matrix composites[J]. Compos Part B Eng, 2022, 243: 110177.

[140] CAI F Y, NI D W, ZHOU Z Y, et al. Ablation mechanism of Cf/($Ti_{0.2}Zr_{0.2}Hf_{0.2}Nb_{0.2}Ta_{0.2}$)C-SiC composite during plasma ablation

above 2000 ℃[J]. J Mater Sci Technol, 2025, 213: 109–117.

[141] MIAO Q, FU Y Q, CHEN H, et al. Simultaneous enhancement of mechanical and ablation properties of C/C composites modified by (Hf-Ta-Zr)C solid solution ceramics[J]. J Eur Ceram Soc, 2023, 43(8): 3182–3190.

[142] FU Y Q, ZHANG Y L, LI T, et al. Effect of SiC on the anti-ablation resistance and flexural strength of (Hf-Ta-Zr)C-C/C composites[J]. J Eur Ceram Soc, 2024, 44(1): 107–118.

[143] GAO S, WANG Y C, HU J R, et al. Ablation behaviour of multi-component (Hf, Zr, Ti)C ceramics modified carbon/carbon composites[J]. J Eur Ceram Soc, 2025, 45(5): 117141.

[144] LONG Q Y, WANG Y L, XIONG X, et al. Growth behavior of (Hf, Zr, Ti)C multicomponent transition metal carbide during melt infiltrating into porous C/C composites[J]. Ceram Int, 2025, 51(8): 10453–10466.

[145] XU J J, SUN W, XIONG X, et al. C/C-($Hf_{0.5}Zr_{0.3}Ti_{0.2}$)C–W–Cu composites: Long-term ablation resistance based on active-passive protection at 2600 ℃[J]. Compos Part B Eng, 2025, 289: 111889.

[146] GUO W J, HU J, FANG W, et al. A novel strategy for rapid fabrication of continuous carbon fiber reinforced (TiZrHfNbTa)C high-entropy ceramic composites: High-entropy alloy *in situ* reactive melt infiltration[J]. J Eur Ceram Soc, 2023, 43(6): 2295–2305.

[147] HE H R, YANG J G, GUO W J, et al. Microstructures and formation mechanism of continuous carbon fiber-reinforced (TiZrHfNbTa)C high-entropy ceramic composites fabricated *via* high-entropy alloy reactive melt infiltration[J]. Ceram Int, 2023, 49(22): 36997–37008.

[148] CAI F Y, NI D W, CHEN B W, et al. Efficient fabrication and properties of 2D Cf/($Ti_{0.2}Zr_{0.2}Hf_{0.2}Nb_{0.2}Ta_{0.2}$)C-SiC high-entropy ceramic matrix composites *via* slurry infiltration lamination combined with precursor infiltration and pyrolysis[J]. J Eur Ceram Soc, 2023, 43(16): 7403–7410.

[149] ZHANG L, WANG W Q, ZHOU N P, et al. Low temperature fabrication of Cf/BNi/($Ti_{0.2}Zr_{0.2}Hf_{0.2}Nb_{0.2}Ta_{0.2}$)C-SiCm high entropy ceramic matrix composite by slurry coating and laminating combined with precursor infiltration and pyrolysis[J]. J Eur Ceram Soc, 2022, 42(7): 3099–3106.

[150] HU Y, NI D W, CHEN B W, et al. Cf@BN/(CrZrHfNbTa)C–SiC high-entropy ceramic matrix composites with outstanding electromagnetic interference shielding and high-temperature resistance[J]. Ceram Int, 2024, 50(20): 38582–38591.

[151] HU Y, NI D W, CHEN B W, et al. Ablation behavior and mechanisms of Cf/(CrZrHfNbTa)C–SiC high-entropy composite at temperatures up to 2450 ℃[J]. J Am Ceram Soc, 2024, 107(12): 8661–8675.

[152] HU Y, NI D W, CHEN B W, et al. Cf/(CrZrHfNbTa)C–SiC high-entropy ceramic matrix composites for potential multi-functional applications[J]. J Mater Sci Technol, 2024, 182: 132–140.

[153] SHEN Y Z, SUN W, XU Y L, et al. Excellent oxyacetylene ablation performance of C/C-Me-Zr-Hf-C (Me=Ta, Si) composites prepared by a novel two-step molten salt infiltration[J]. J Eur Ceram Soc, 2024, 44(5): 3084–3098.

[154] DONG Z J, LIU B, HU D, et al. Low-temperature preparation of C/C-W-Cu composites with enhanced particle impact and ablation resistance[J]. J Alloys Compd, 2025, 1010: 177605.

[155] GUO W J, GONG J Y, ZHU L A, et al. Oxidation and ablation resistance of (TiZrHf)C medium-entropy ceramic coating on C/C composite constructed *in situ* at low temperature down to 900 ℃[J]. J Eur Ceram Soc, 2025, 45(3): 116976.

[156] HU D, FU Q G, ZHOU L, et al. Effects of air plasma flame on the $ZrB_2$-based UHTC coatings: Microstructure, phase evolution and ablation resistance[J]. J Mater Sci Technol, 2023, 158: 194–206.

[157] LI J C, ZHANG Y L, FU Y Q, et al. Twin toughening-driven martensitic transformation strategy synergistic improvement for plasticity-thermal shock resistance of (Hf–Zr–Ti)C ceramic coating in severe thermal environments[J]. Adv Sci, 2025, 12(26): 2503226.

[158] ZHANG J H, LI T, FU Y Q, et al. Ablation resistance of ($Hf_{1/3}Zr_{1/3}Ta_{1/3}$)C solid solution ceramic coating for carbon/carbon composites at 2100 ℃[J]. Ceram Int, 2024, 50(22): 45232–45241.

[159] LI X X, ZHANG M L, HU D, et al. Long-term performance optimization on (Hf-Zr-Ta-Nb)C coatings above 2000 ℃: Element, composition and ablation property[J]. J Eur Ceram Soc, 2025, 45(12): 117403.

[160] GUO L X, HUANG S W, LI W, et al. Theoretical design and experimental verification of high-entropy carbide ablative resistant coating[J]. Adv Powder Mater, 2024, 3(5): 100213.

[161] ZHANG J, ZHANG Y L, FU Y Q, et al. Research progress in chemical vapor deposition for high-temperature anti-oxidation/ablation coatings on thermal structural composites[J]. Compos Part B Eng, 2025, 291: 112015.

[162] ZHANG J, ZHANG Y L, CHEN R C, et al. Ablation behavior of a novel carbonitrides HfC0.68N0.32 coating for C/C composites in laser and oxyacetylene environment[J]. J Eur Ceram Soc, 2024, 44(5): 3049–3057.

[163] ZHANG J, ZHANG Y L, CHEN R C, et al. Effect of microstructure on the ablation behavior and mechanical properties of CVD-HfC coating[J]. Corros Sci, 2021, 192: 109815.

[164] ZHANG J, ZHANG Y L, FU Y Q, et al. Growth mechanism and ablation behavior of CVD-HfC coating on the surface of C/C composites and CVD-SiC coating[J]. Corros Sci, 2021, 192: 109819.

[165] ZHANG J, ZHANG Y L, FU Y Q, et al. Long-time ablation behavior of the multilayer alternating CVD-$(SiC/HfC)_3$ coating for carbon/carbon composites[J]. Corros Sci, 2021, 189: 109586.

[166] ZHANG J, ZHANG Y L, ZHU X F, et al. Design and preparation of multilayer TaC/HfC coating: Ablation behavior under oxyacetylene flame with different heat flux[J]. Corros Sci, 2022, 204: 110385.

[167] CHEN R C, ZHANG Y L, ZHANG J, et al. $MoSi_2$ modified HfC coating for the ablation protection of SiC-coated C/C composites: Ablation resistance and behavior[J]. Corros Sci, 2022, 205: 110418.

[168] KONG J A, ZHANG Y L, CHEN G H, et al. Ablation behavior of CVD-TaC coatings with different crystal structures for C/C composites under oxyacetylene flame[J]. J Eur Ceram Soc, 2022, 42(15): 6898–6907.

[169] KONG J A, ZHANG Y L, GAI W H, et al. Influence of crystallite morphology on the ablative behaviors of CVD-TaC coatings prepared on C/C composites beyond 2100 ℃[J]. Corros Sci, 2022, 205: 110426.

[170] KONG J A, ZHANG Y L, WANG H H, et al. Sublayer design and ablation resistance of CVD-TaC alternate coatings with different crystallite morphologies for C/C composites[J]. J Mater Sci Technol, 2023, 141: 1–10.

[171] CHEN H, ZHANG Y L, FU Y Q, et al. Novel $Hf_xTa_{1-x}C$ solid solution nanowire toughened HfC coating: An effective strategy for synchronous enhanced mechanical and anti-ablation performance[J]. J Adv Ceram, 2024, 13(5): 590–601.

[172] CHEN H, ZHANG Y L, LI Z L, et al. Ablation behavior of HfC coatings modified by novel $Hf_xTa_{1-x}C$ solid solution nanowires under oxyacetylene flame[J]. Ceram Int, 2024, 50(6): 9668–9677.

[173] CHEN H, ZHANG Y L, FU Y Q, et al. $(Hf_{0.5}Ta_{0.5})C$ ultra-high temperature ceramic solid solution nanowires[J]. J Mater Sci Technol, 2023, 147: 91–101.

[174] CHEN H, ZHANG Y L, LI Z L, et al. Ultra-high temperature ablation behavior of CVD-$Hf_5TaC_6$ solid solution ceramic coating for C/C composites: Experiment and first-principle calculation[J]. J Alloys Compd, 2023, 965: 171486.

# Development on Medium-/High-Entropy Carbide Ceramics and Their Substrate/Coating-Modified C/C Composites

*LI Jiachen*[1], *ZHANG Yulei*[1,2], *LI Tao*[2], *ZHANG Jian*[1], *FU Yanqin*[2], *LV Junshuai*[1], *LI Hejun*[1]

(1. State Key Laboratory of Ultra-High Temperature Structural Composites, Northwestern Polytechnical University, Xi'an 710072, China; 2. Henan Key Laboratory of High Performance Carbon Fiber Reinforced Composites, Institute of Carbon Matrix Composites, Henan Academy of Sciences, Zhengzhou 450046, China)

## Extended Abstract

Improving the ablation resistance of C/C composites under ultra-high temperature environments is a prerequisite for their applications as thermal protection components in high-speed aircraft. When conventional silicide-modified C/C composites serve in an aerobic environment at >1700 ℃, the active oxidation of silicide is intensified, causing the formation and escape of gaseous SiO from unoxidized silicide. Concurrently, the decomposition pressure and saturation vapor pressure of $SiO_2$ increase with temperature, accelerating their decomposition and volatilization from the oxide scale. These processes lead to a rapid consumption of silicide, preventing the formation of a dense and continuous oxygen barrier, and resulting in a gradual loss of thermal protection capability.

Among ultrahigh-temperature ceramics (UHTCs), HfC and ZrC are preferred modified components for their high melting points (>3000 ℃) and good chemical stability, as well as high melting points of their oxidation products (*i.e.*, $HfO_2$: 2810 ℃ and $ZrO_2$: 2677 ℃). Nevertheless, their protective oxide scales exhibit a loose structure after long-term oxidation/ablation due to the lack of a densification pathway capable of healing oxidation/ablation-induced defects (pores and cracks). To mitigate this issue, the liquid-phase sintering effect of low-melting oxide phases (*i.e.*, $TiO_2$: ~1840 ℃, $Ta_2O_5$: ~1800 ℃, and $Nb_2O_5$: ~1512 ℃) promotes their solid solution process with high-melting $HfO_2$/$ZrO_2$ and produces dense Hf/Zr-X-O compound (X=Ti, Ta and Nb), healing ablative defects during ablation. As a result, the ablation resistance of the coatings is significantly improved. Consequently, some multi-phase carbides are widely applied for C/C composites, including HfC-ZrC-TiC, HfC-TaC, ZrC-TaC, HfC-ZrC-TaC, HfC-NbC, and ZrC-NbC. However, they are typically prepared by mechanical blending through ball milling before spraying, showing an inhomogeneous elemental distribution in a microscale. It induces locally aggregated low-melting phases, having an insufficient mechanical denudation resistance, thus impeding further improvement of ablation resistance. Conventional silicide- and multi-phase carbide ceramic-modified C/C composites face some challenges, including insufficient high-temperature stability, limited long-term ablation resistance, and narrow protective temperature ranges.

In comparison to these ceramics, medium-/high-entropy carbide (M/HEC) ceramics unique “four effects” and tunability of composition and microstructure endow excellent comprehensive properties. This review represented the preparation methods of M/HEC ceramics, which are composed of solid-phase reaction (*i.e.*, Carbothermal reduction method, Direct synthetic method, and Molten salt synthesis) and liquid-phase reaction (*i.e.*, Polymer-derived ceramics and Sol-gel) methods, and discussed their effects on the structure and properties of M/HEC ceramics. The preparation methods of M/HEC substrate-modified C/C (*i.e.*, Precursor infiltration and pyrolysis, Reaction melt infiltration, and Molten salt infiltration methods) and M/HEC coating-modified C/C (*i.e.*, Supersonic atmospheric plasma spraying method) were described, and the preparation cycles of different processes and their effects on the structure and properties of C/C composites were compared. Finally, the influence of different M/HEC on the ablation resistance was summarized, and some promising prospects for the future development of M/HEC substrate/coating-modified C/C composites were proposed.

**Summary and Prospects**　The focus and difficulties of M/HEC substrate/coating-modified C/C in future work mainly include the following aspects:

1) Efficient and rapid design of anti-oxidation/ablation ceramic components. With the rapid advancement of “Artificial Intelligence+Materials” and the proposal of the “Materials Genome Initiative”, an increasing number of computational methods, integrated computing platforms, and databases are developed. This progress enables the use of AI-based high-throughput theoretical calculations (*i.e.*, thermodynamics, finite element, first principles calculations, and molecular dynamics) and experimental verification to establish the M/HEC performance databases and optimize the M/HEC components with the superior comprehensive performance.

2) Construction of substrate/coating and their microstructure control. The structural designs (*i.e.*, M/HEC zoned gradient modification, M/HEC nano-reinforcements, and M/HEC gradient coatings), stress distribution simulations (*i.e.*, at interface and within gradient sublayer), and multi-scale heterogeneous interface control can improve the interface bonding and stress distribution state between M/HEC and C/C substrates, leading to a synergistic enhancement in bonding strength, crack suppression, and ablation resistance.

3) Clarifying the oxidation/ablation protection mechanisms under extreme coupling environments involving thermal, mechanical, and medium factors. A comprehensive service environment evaluation system, such as the plasma or arc wind tunnel, should be used to simulate multi-field conditions, including thermal exposure, mechanical loads (*i.e.*, high-speed airflow and particle erosion), and corrosive medium (*i.e.*, oxygen and water vapor). An in-situ visualization system is used to monitor the long-term service stability of M/HEC substrate/coating modified C/C composites under extreme service environments, which involve ultra-high temperature oxidation/ablation, high- and low-temperature thermal impact, and strong airflow denudation. In addition, multi-scale theoretical calculations and advanced in-situ characterization techniques are conducted to elucidate their oxidation/ablation protection mechanisms.

4) Fabrication of large-sized components and acceleration of their engineering applications. The existing preparation of M/HEC substrate/coating modified C/C composites remains largely confined to laboratory-scale research. Producing large-sized components is a complex process, which requires a large-scale processing equipment and precisely controls over multiple steps to achieve uniform distribution of M/HEC internally and externally throughout the entire structure. It is urgent for overcoming the application bottlenecks of process stability, composition uniformity, stress control and structural/functional integration design of large-sized components to develop simple and efficient preparation techniques.

**Keywords** carbon/carbon composites; medium/high-entropy carbide; substrate/coating modification; ablation resistance